## Energy Spectra and Vorticity Dynamics in a Two-Layer Shallow Water Ocean Model

NICHOLAS K.-R. KEVLAHAN<sup>a</sup> AND FRANCIS J. POULIN<sup>b</sup>

<sup>a</sup> Department of Mathematics and Statistics, McMaster University, Hamilton, Ontario, Canada <sup>b</sup> Department of Applied Mathematics, University of Waterloo, Waterloo, Ontario, Canada

(Manuscript received 23 December 2021, in final form 5 July 2022)

ABSTRACT: The dynamically adaptive WAVETRISK-OCEAN global model is used to solve one- and two-layer shallow water ocean models of wind-driven western boundary current (WBC) turbulence. When the submesoscale is resolved, both the one-layer simulation and the barotropic mode of the two-layer simulations have an energy spectrum with a power law of -3, while the baroclinic mode has a power law of -5/3 to -2 for a Munk boundary layer. This is consistent with the theoretical prediction for the power laws of the barotropic and baroclinic (buoyancy variance) cascades in surface quasi-geostrophic turbulence. The baroclinic mode has about 20% of the energy of the barotropic mode in this case. When a Munk–Stommel boundary layer dominates, both the baroclinic and barotropic modes have a power law of -3. Local energy spectrum analysis reveals that the midlatitude and equatorial jets have different energy spectra and contribute differently to the global energy spectrum. We have therefore shown that adding a single baroclinic mode qualitatively changes WBC turbulence, introducing an energy spectrum component typical of what occurs in stratified three-dimensional ocean flows. This suggests that the first baroclinic mode may be primarily responsible for the submesoscale turbulence energy spectrum of the oceans. Adding more vertical layers, and therefore more baroclinic modes, could strengthen the first baroclinic mode, producing a dual cascade spectrum (-5/3, -3) or (-3, -5/3) similar to that predicted by quasigeostrophic and surface quasigeostrophic models, respectively.

SIGNIFICANCE STATEMENT: This research investigates how wind energy is transferred from the largest ocean scales (thousands of kilometers) to the small turbulence scales (a few kilometers or less). We do this by using an idealized model that includes the simplest representation of density stratification. Our main finding is that this simple model captures an essential feature of the energy transfer process. Future work will compare our results to those obtained using ocean models with more realistic stratifications.

KEYWORDS: Barotropic flows; Turbulence; Energy budget/balance; Vorticity; Adaptive models; Numerical analysis/modeling

#### 1. Introduction

#### a. Energy dynamics in the ocean

The winds continually force the oceans from above, providing much of the energy that drives the oceanic circulation (Wunsch 1998). The large-scale wind-driven gyres that develop are a horizontal structure that arises because of the wind forcing. This is in contrast to the meridional overturning circulation (MOC), which is essentially a vertical structure (Vallis 2006) and is driven by significant buoyancy fluxes. One of the central questions of ocean physics is how the barotropic two-dimensional gyres generate and interact with the three-dimensional baroclinic vertical structure of the oceans. How is energy transferred from the large-scale two-dimensional barotropic mode to the small-scale three-dimensional baroclinic modes? This can happen in a variety of ways, and some of these mechanisms are nonintuitive (Straub and Nadiga 2014). This energy transfer, in turn, depends on differences between the barotropic energy at the mesoscale and the baroclinic energy at smaller scales.

Our goal in this paper is to explore the effect of including a single baroclinic component by comparing results from

Corresponding author: Nicholas K.-R. Kevlahan, kevlahan@mcmaster.ca

numerical simulations of one- and two-layer global shallow water ocean models with simplified western boundary geometry. The simulations are performed using the dynamically adaptive model WAVETRISK-OCEAN (Kevlahan 2021; Kevlahan and Lemarié 2022). We are particularly interested in characterizing the vorticity dynamics and energy spectrum of barotropic and baroclinic turbulence in the western boundary currents (WBC).

Cox and Bryan (1984) made an early attempt to resolve the three-dimensional dynamics arising from the atmospheric winds. Since then, many others have worked to better understand the structure and dynamics of both the horizontal and vertical motions of wind-driven ocean circulation (e.g., Steele et al. 2001; Jackson et al. 2006; Corre et al. 2020). The simplest way to include baroclinicity is to use either a two-layer or two-vertical mode system (Phillips 1954). Stewart et al. (2021) is an example of recent work that uses a two-layer model to investigate the importance of bottom topography on the development of the gyre.

A two-layer model allows us to focus on the leading-order physical effects associated with vertical density gradients. In other words, it allows us to answer the question: which new physical effects are introduced by adding a single baroclinic mode? Which effects require more vertical structure?

Since the pioneering work of Stommel (1948) and Munk (1950), it is well understood that wind-driven gyres generate

DOI: 10.1175/JPO-D-21-0318.1

TABLE 1. Energy spectrum power laws for different models of forced turbulence. Note that p = -2 is typical for near-surface ocean turbulence, characterized by mixed layer instabilities (Callies and Ferrari 2013) and for wave turbulence (Garrett and Munk 1972, 1975).

| Model                    | Power law $p$ , $E(k) \propto k^p$ | Interpretation                        | Reference                  |
|--------------------------|------------------------------------|---------------------------------------|----------------------------|
| 3D homogeneous isotropic | -5/3                               | Forward energy cascade                | Kolmogorov (1991)          |
| 2D homogeneous isotropic | -5/3 large scale                   | Inverse energy cascade                | Batchelor (1969)           |
|                          | −3 small scale                     | Forward enstrophy cascade             |                            |
| Quasigeostrophy          | -5/3 large scale                   | Inverse energy cascade                | Salmon (1998)              |
|                          | −3 small scale                     | Forward enstrophy cascade             |                            |
| Surface quasigeostrophy  | −3 large scale                     | Inverse 2D barotropic energy cascade  | Tulloch and Smith (2009)   |
|                          | -5/3 small scale                   | Forward 3D buoyancy variance cascade  |                            |
| Internal wave turbulence | -2                                 | Wave turbulence                       | Garrett and Munk (1975)    |
|                          | -2.5                               | Long internal wave turbulence         | Lvov and Tabak (2001)      |
| Numerical ocean          | -2                                 | Dominant submesoscale                 | Morvan et al. (2020)       |
|                          | -4                                 | Dominant mesoscale eddies             |                            |
| Real ocean               | 0 to $-3$                          | Jason-1/2 surface kinetic energy data | Callies and Ferrari (2013) |
|                          |                                    |                                       | Xu and Fu (2011, 2012)     |

western intensification in the form of WBC. WBC form because ocean gyres transport as much mass poleward as they do equatorward, but part of this transport occurs in a very narrow region along the western boundary. This is of great interest because WBC are the most energetic large-scale features of the ocean (Wunsch 1998) and contribute significantly to the cross Atlantic transport of momentum, heat, and biogeochemistry (Flierl and Davis 1993). Their structure is characterized by intense mesoscale coherent vortices (i.e., eddies) and turbulence. WBC distribute energy across a wide range of spatial scales, from laminar flow at the large barotropic basin scales to turbulence at the submesoscales. Idealized two- and three-dimensional turbulence theory has been used to better understand the nature of the oceans in these rich and complex flows. There are many such turbulence models, and different models can yield very different behaviors. Conversely, different turbulence models may yield the same inertial range power law scaling.

The principal goal of this paper is to compare power law scaling for the barotropic and baroclinic turbulence modes in a two-layer shallow water WBC simulation in order to determine what kind of dynamics can occur with the addition of a single baroclinic mode.

## b. Review of geophysical turbulence models and observations

Many current models of turbulence rely on Kolmogorov's (1991) description of homogeneous isotropic incompressible three-dimensional turbulence at very high Reynolds numbers. Kolmogorov's insight was that at large Reynolds numbers there should be an "inertial range" of wavenumbers larger than the wavenumbers where energy is injected and smaller than the wavenumbers where viscosity dissipates energy. In the inertial range the dynamics are scale independent, and energy is transferred from small to large wavenumbers by the nonlinear term of the Navier–Stokes equation. Dimensional analysis then shows that the energy spectrum in the inertial range should follow a power law  $E(k) \propto k^p$ , with p = -5/3. This prediction was verified to high accuracy from observations of a tidal channel

by Grant et al. (1962). Subsequent theories of turbulence in other configurations (two-dimensional, quasigeostrophic, stratified, etc.) rely on the same general approach of identifying inertial ranges characterized by a conserved quantity, such as kinetic energy or enstrophy.

Table 1 summarizes the spectral slopes associated with different mathematical models, numerical simulations, and observations. We conclude that, depending on the underlying physics, turbulence is characterized by two types of spectral slopes: a shallow -5/3 to -2.5 slope and a steeper slope of -3 to -4. Both slopes are observed in the oceans, depending on local conditions.

Two-dimensional dissipative turbulence forced at an intermediate scale has a dual cascade, where the inverse cascade of energy has a -5/3 scaling at larger scales and the forward cascade of enstrophy has a -3 at small scales. Numerical simulations typically find a small-scale slope between -3 and -4, where -3 is believed to be the asymptotic limit for large Reynolds numbers (Boffetta and Musacchio 2010). Decaying two-dimensional turbulence has a single power law of about -3.

Part of the motivation for studying two-dimensional turbulence is that the large-scale dynamics of the ocean are approximately two-dimensional because of strong density stratification and rapid rotation of Earth. However, even though the oceans can sometimes be approximated by two-dimensional flows at large scales, the smaller scales are three-dimensional, and these give rise to very complicated features like the MOC (Vallis 2006) that cannot be represented in a simple barotropic, two-dimensional model.

Geostrophic turbulence is turbulence that is close to geostrophic and hydrostatic balance, which requires small Froude, Ekman, and Rossby numbers (Salmon 1998). The barotropic (two-dimensional) quasigeostrophic (QG) model is often used to study geostrophic turbulence, as it is computationally less expensive than studying primitive equation models. It has been demonstrated that the spectral slopes obtained from a QG turbulence model are essentially the same as what is observed in the simpler case of two-dimensional turbulence (Salmon 1998). This then suggests that the interior dynamics of large-scale

ocean flows should have the same spectra as two-dimensional turbulence.

The surface quasigeostrophic (SQG) model is different from the OG model in that it is designed to describe oceanic flows at the surface, or possibly at the bottom. It is well known that the SQG model has very different physical behavior from QG model and, as a result, produces different spectra (Tulloch and Smith 2009; Lapeyre 2017; Callies and Ferrari 2013). In particular, Tulloch and Smith (2009) have shown that forced SQG turbulence can give rise to the opposite scenario of 2D and QG turbulence: the large scales have a slope of -3 and the small scales have a slope of -5/3. This is of great physical interest because this spectrum has been observed in the atmosphere (Nastrom and Gage 1985). In the subtropical North Pacific, there is a strong surface buoyancy gradient and even though one might expect SQG (surface) turbulence dynamics, this was not found by Callies and Ferrari (2013). To the best of our knowledge, this is an outstanding issue that has yet to be resolved.

Observations in the Gulf Stream have demonstrated that both QG and SQG models are appropriate models for describing interior and near-surface dynamics, respectively (Callies and Ferrari 2013). It was determined from observations of the Gulf Stream that the QG (interior) turbulence dominated the observations at length scales larger than 20 km. At smaller scales internal waves became important and yielded a slope closer to -2, typical of a mixed layer instability.

There are far fewer investigations of turbulence in the onelayer shallow water model, compared to the Boussinesq or QG models. An early investigation is by Yuan and Hamilton (1994), which explored equilibrium states in the context of a one-layer forced-dissipative f-plane shallow water model. By decomposing the flow into rotational and divergent components, they determined that the rotational component is similar to the enstrophy cascade of two-dimensional turbulence, where the energy spectrum has a power law of -3. The divergent part, which consists of the inertia-gravity waves, has a power law of -3 at large scales, but with a shallower tail at smaller length scales, which is related to the mesoscale in the atmosphere or submesoscale in the ocean. The authors conclude that the presence of inertia-gravity waves can give rise to shallower slopes at small scales in the forced-dissipative shallow water model. Afanasyev and Craig (2013) also found slopes of -5/3 at large scales and -3 and smaller scales in the total energy spectra (like 2D turbulence), which suggests that inertia-gravity waves were very strong compared to the slower balanced motions. This is different from previous observations, which may be due to the fact that they use charged fluids.

Cho and Polvani (1996) investigated freely evolving onelayer shallow water turbulence on a sphere with no continents. They confirmed previous results by Yoden and Yamada (1993), that the flow tends to a vorticity quadrupole when there is a rigid lid and a flat bottom. The presence of a free surface (finite Rossby radius of deformation) gave rise to a banded structure. This could occur in their model since no continents were included. Many of their simulations had spectral slopes of -3, but they did find some slopes close to -1.8occurred at the large scales before the vorticity quadrupole emerged. This study was extended to include forced-dissipative turbulence in Scott and Polvani (2007). They found that for large radii of deformation (compared to the radius of the planet), the width of the zonal jets is well approximated by the Rhines scale (Rhines 1975). As well, they find that prograde and retrograde jets can occur at the equator with equal degree of likelihood. For smaller radii of deformation, the equatorial jets become consistently retrograde, which agrees with Theiss (2004). Kitamura and Ishioka (2007) did similar experiments of freely decaying one-layer, shallow water turbulence on a sphere without any continents. They show that a Rossby wave packet propagating toward the equator tends to include retrograde acceleration of the equatorial jet.

#### c. Similar studies and physical models

Barotropic models of turbulence, such as the two-dimensional turbulence model, are necessarily limited in the ocean physics they can describe. Stratification (i.e., baroclinicity and three-dimensional structure) can be introduced in ocean models in a variety of ways (Phillips 1963). Using the terminology of Beron-Vera (2021), we can classify baroclinic ocean models as

- layered—horizontally homogeneous density layers (e.g., an n-HL<sup>0</sup> model, which has homogeneous density layers with no vertical variation within each layer);
- 2) levels—horizontally inhomogeneous density layers (e.g., an *n*-IL<sup>0</sup> model, which has inhomogeneous density layers with no vertical variation within each layer); and
- modal—decomposition based on the vertical structure of the normal modes.

Each of these models is different, but can yield similar results. WAVETRISK-OCEAN is a hydrostatic *n*-IL<sup>0</sup> level model, but it is run here as a 2-HL<sup>0</sup> model (i.e., with two, constant density, layers). Modal models have been developed primarily for idealized studies (Fu and Flierl 1980).

The hydrostatic approximation restricts the types of motions that can be described accurately. In particular, they are restricted to studying motions with a large aspect ratio,  $H/L \ll 1$ , i.e., the motions must have a long horizontal length scale compared to their vertical length scale. This restriction holds for all multilayer shallow water models. In nonhydrostatic models it is often the case that the aspect ratio is chosen such that  $H/L \sim f/N$ , the ratio of the Coriolis and buoyancy frequencies. It has been shown in Nadiga (2014) that when this is not done, spurious motions can occur. This is not something that we need to address because of the relative simplicity of our model, but it is a limitation shared by all multilayer hydrostatic ocean models.

Lapeyre and Klein (2006) simulated the upper ocean using a high-resolution three-dimensional numerical model. This model allows strong restratification, which is not permitted in either QG or SQG. They observed a shallow slope of -2 in the velocity spectrum. Therefore, even though SQG should not strictly be valid in this regime, it does yield results that are consistent with the surface dynamics of the ocean. They state that QG turbulence is characterized by

- a steep energy spectrum with power laws close to −3 or −4 at large wavenumbers,
- 2) a direct cascade of baroclinic (potential) energy, and
- 3) an inverse cascade of barotropic energy from scales close to the Rossby radius of deformation to large scales with a power law close to -5/3 at small wavenumbers.

Furthermore, Smith and Vallis (2001), who decomposed the flow into vertical modes, show that surface-intensified stratification slows the transition from the baroclinic to barotropic mode, as a result of baroclinic instability. They suggested that the first baroclinic mode includes these surface-intensified motions typical of three-dimensional flows. Fu and Flierl (1980) show an example where higher-order baroclinic modes transfer some of their energy to the first baroclinic mode.

Favier et al. (2019) is quite close in goals and conception to our two-layer model, but in a different physical context. They studied the turbulence dynamics that develops in rotating Rayleigh-Bénard convection. They computed the two- and three-dimensional portions of the flow, which in our context we call the barotropic and baroclinic components of the flow. They found that the baroclinic (three-dimensional) and barotropic (two-dimensional) components each had power law of -5/3 and -3, respectively, for the same range of wavenumbers. However, the baroclinic component was more energetic. In our work we study a different physical problem, the spinup of the wind driven gyres, using a very different physical approximation and numerical model. However, our barotropicbaroclinic decomposition is similar to Favier et al.'s (2019) two-dimensional/three-dimensional decomposition and we also find that the baroclinic and the barotropic flows have slopes of -5/3 and -3, respectively. One major difference is that we consider a two-layer model, and therefore there is only a single baroclinic mode, unlike Favier et al. (2019), who have a much better resolved vertical coordinate, which is presumably what produces much more energy in the baroclinic models. We speculate that with a fully three-dimensional ocean model, we would find that the baroclinic modes still have slopes of -5/3, but with energy content similar to the barotropic mode. However, a multilayer simulation is beyond the scope of this paper (and complicates the interpretation of the results) and therefore this question is reserved for future work.

These results suggest that the first baroclinic mode, which we include in our two-layer model, is the most important of all the baroclinic modes for understanding ocean turbulence.

### d. Outline of the paper and its contributions

In this manuscript, we study the evolution of wind-driven gyre flows in a two-layer shallow water model. We solve the two-layer shallow water model on the sphere with an idealized Drake Passage topography using the WAVETRISK-OCEAN code. The dynamic adaptivity of this code permits very high local resolutions where required to resolve the submesoscale dynamics. To further maximize resolution, we consider a small planet, 1/6 Earth's diameter. To the best of our knowledge, this is the first investigation of a wind-driven shallow water ocean model that includes idealized continents.

We decompose the flow into its barotropic and baroclinic components, as described in section 2c. The barotropic and baroclinic components of the results are diagnosed to understand how they differ. This is done by comparing their respective vorticity fields in physical space, as well as by computing their spherical harmonic energy spectra (and extracting their associated inertial range power laws). This barotropic–baroclinic decomposition is commonly used for rotating convection (Julien et al. 2012; Rubio et al. 2014; Julien et al. 2018; Favier et al. 2019).

In section 2 we present the model equations, the equations for the evolution of energy, the barotropic–baroclinic decomposition, the numerical method used to simulate the flow, the tools used for the spectral analysis, and the details of the model configuration. Details of the setup and different scenarios are given in section 2g. In section 3 we discuss the vorticity plots obtained from our simulations obtained for the various simulations (one-layer/two-layer, fast/normal/slow rotation, weak/strong baroclinic mode). Section 4 presents the energy spectra computed for the cases shown in section 3. Finally, in section 5 we summarize and interpret our main results.

Our results show that both the one-layer simulation and the barotropic component of the two-layer simulation have an energy spectrum with a power law of -3, while the weaker threedimensional baroclinic flow has a power law of -5/3 to -2 in the presence of a Munk boundary layer. These results are similar to those found for rotating stratified flows. We therefore demonstrate that adding a single baroclinic mode qualitatively changes the turbulence, introducing a spectral component observed in three-dimensional ocean flows. Large bottom friction, which produces a Munk-Stommel boundary layer, generates a dominant baroclinic mode and steepens the baroclinic energy spectrum compared to the weak baroclinic mode cases. The terms "Munk layer" and "Munk-Stommel layer" are defined in section 2g. We interpret the spectral results in terms of different types of vortical structures (i.e., coherent eddies and filamentary turbulence) by computing local energy spectra in different parts of the ocean (e.g., in the midlatitude current and equatorial jet of the WBC).

#### 2. Idealized ocean model

#### a. Model equations

In this investigation we focus on the two-layer shallow water model with a free surface and a flat bottom. As is well known, the dynamics of the free surface and the layer interfaces are strongly coupled to the barotropic and baroclinic dynamics, respectively. The governing equations for the multilayer shallow water model can be found in Vallis (2006) for cases with and without a free surface. The dynamical equations in our two-layer case with a free surface are

$$\begin{split} \partial_{t}\mathbf{u}_{1} + \nabla \frac{1}{2}|\mathbf{u}_{1}|^{2} + q_{1}h_{1}\mathbf{u}_{1}^{\perp} &= -(g - g')\nabla h + \frac{\tau}{\rho_{0}h_{1}} \\ &- r_{1}(\mathbf{u}_{1} - \mathbf{u}_{2}) + \nu\Delta\mathbf{u}_{1}, \end{split} \tag{1}$$

$$\begin{split} \partial_{t}\mathbf{u}_{2} + \nabla \frac{1}{2}|\mathbf{u}_{2}|^{2} + q_{2}h_{2}\mathbf{u}_{2}^{\perp} &= -g\nabla h + g'\nabla h_{1} - r_{b}\frac{\mathbf{u}_{2}}{h_{2}} \\ &- r_{2}(\mathbf{u}_{2} - \mathbf{u}_{1}) + \nu\Delta\mathbf{u}_{2}, \end{split} \tag{2}$$

$$\partial_{i}h_{1} + \nabla \cdot (h_{1}\mathbf{u}_{1}) = 0,$$
 (3)  $\partial_{i}h + \nabla \cdot (h\mathbf{u}) = 0.$ 

$$\partial_t h_2 + \nabla \cdot (h_2 \mathbf{u}_2) = 0, \tag{4}$$

where  $\mathbf{u}_i(\mathbf{x}, t)$  and  $h_i(\mathbf{x}, t)$  are the horizontal velocities and thicknesses of layer i, for i = 1, 2 (top and bottom layers, respectively) with total depth  $h = h_1 + h_2$ . The mean layer depths are  $H_i$ , with  $H = H_1 + H_2$  the total mean depth. The Coriolis term f is included in the potential vorticity  $q_i = (\hat{\mathbf{z}} \cdot \nabla \times \mathbf{u}_i + f)/h_i$ , where  $\hat{\mathbf{z}}$  is the local unit normal to the sphere, and the rotated horizontal velocity  $\mathbf{u}_{i}^{\perp} = \hat{\mathbf{z}} \times \mathbf{u}_{i}$ . The term  $\tau$  is the wind stress, g is the gravitational acceleration,  $g' = g(\rho_2 - \rho_1)/\rho_0$  is the reduced gravity,  $r_b$  is the bottom friction coefficient,  $r_i$  is internal wave friction, and  $\nu$  is the lateral viscosity. We set  $\rho_0 = \rho_2$ . As explained in section 2c, the wind stress, bottom drag, and internal drag are incorporated in the discretization of the Laplacian vertical diffusion. The horizontal Laplacian diffusion terms can be thought of as a simple model for horizontal turbulence with a constant turbulent viscosity  $\nu$  much larger than the molecular viscosity of water.

We compare the two-layer results with results from a simulation of the single layer shallow water equations

$$\partial_t \mathbf{u} + \nabla \frac{1}{2} |\mathbf{u}|^2 + qh\mathbf{u}^{\perp} = -g\nabla h + \frac{\tau}{\rho_0 h} - r_b \frac{\mathbf{u}}{h} + \nu \Delta \mathbf{u},$$
 (5)

is not the same as the barotropic mode of the two-layer system.

Energy is added to the system via wind stress at the free surface (i.e., distributed over the top layer) and is then diffused horizontally due to lateral viscosity in both layers. Bottom friction removes energy from the system and redistributes energy between the barotropic and baroclinic modes. The internal drag transfers momentum from the faster layer (typically the top) to the slower layer (typically the bottom) and is a two-layer version of Laplacian vertical diffusion of momentum [see Eqs. (11) and (12)]. Furthermore, the pressure gradients are an important means through which energy can be transferred between the two layers. Both horizontal layers evolve due to nonlinear advection, Coriolis pseudoforce, hydrostatic pressure gradient, interior drag, and lateral viscosity. Mass is conserved separately in each layer and the density is constant in each layer.

#### b. Energetics

We can use standard approaches, as explained in Vallis (2006), to obtain an evolution equation for the total energy density of the two-layer system and it yields the following:

$$\frac{\partial_{t} \left( \frac{1}{2} \rho_{0} h_{1} u_{1}^{2} + \frac{1}{2} \rho_{0} h_{2} u_{2}^{2} + \frac{1}{2} g \rho_{1} h_{1}^{2} + \frac{1}{2} g \rho_{2} h_{2}^{2} + g \rho_{1} h_{1} h_{2} \right) = -\nabla \cdot \left[ \mathbf{u}_{2} \left( \frac{1}{2} \rho_{0} h_{2} u_{2}^{2} + g \rho_{2} h_{2}^{2} + g \rho_{1} h_{1} h_{2} \right) \right] + \mathbf{u}_{1} \left( \frac{1}{2} \rho_{0} h_{1} u_{1}^{2} + g \rho_{1} h_{1}^{2} + g \rho_{2} h_{1} h_{2} \right) \right] + \rho_{1} h_{1} \mathbf{u}_{1} \cdot \mathbf{F}_{1} + \rho_{2} h_{2} \mathbf{u}_{2} \cdot \mathbf{F}_{2}, \tag{7}$$

where  $\mathbf{F}_i$  are the terms arising from the vertical diffusion and lateral diffusion. The terms in the bracket following the time derivative are the kinetic and potential energy densities for layer one, then the same terms for layer two, and finally there is a potential energy density due to the coupling of the two layers. The term that contains a divergence is due to the flux of energy due to advection, and these terms make no net contribution to the change in energy if there is no energy added through the boundaries. The final two terms describe how the total energy density changes in time due to the nonconservative forces included in the model, mentioned above.

The energetics is slightly different from that used in Vallis (2006) and other textbooks because we have not approximated one of the densities with the other, and instead used the densities as they appear in the original dynamical equations. Making the approximation in Vallis (2006) only conserves energy to leading order. The resulting error is proportional to the difference in the densities of the two layers.

#### c. Barotropic-baroclinic decomposition

A principal goal of this work is to investigate the additional dynamics that arise in a two-layer system compared to a single-layer shallow water model. A two-layer system is one of

the simplest models that includes some baroclinic effects (i.e., a single baroclinic mode). What sort of new dynamics does this simple model permit? How is the energy spectrum affected? To aid our analysis we decompose the velocity into its barotropic and baroclinic components, where the former is for the whole system and the latter is layer dependent.

The barotropic (BT) velocity  $\overline{\mathbf{u}}$  is defined as the vertical, weighted average of the velocity field,

$$h\overline{\mathbf{u}} = h_1 \mathbf{u}_1 + h_2 \mathbf{u}_2, \tag{8}$$

where  $h = h_1 + h_2$  is the total depth. The barotropic velocity approximates the velocity field in a single layer shallow water system (although it will not be identical to a true single layer model).

The baroclinic (BC) velocity in each layer **u**' is then defined as the difference between the layer velocity and the BT velocity. Using the above equation, the two fields can be written as

$$h\mathbf{u}_1' = h_2(\mathbf{u}_1 - \mathbf{u}_2), \tag{9}$$

$$h\mathbf{u}_2' = h_1(\mathbf{u}_2 - \mathbf{u}_1). \tag{10}$$

We make extensive use of the decomposition (8) and (10) to analyze the results of the simulations. The barotropic velocity  $\overline{\mathbf{u}}$  of the two-layer equations (1) and (4) is not the same as the solution  $\mathbf{u}$  of the single layer shallow water equations (5) and (6), although we will see that its qualitative features are similar.

#### d. Numerical method

The two-layer model described in the previous section is solved on the sphere using WAVETRISK-OCEAN (Kevlahan and Lemarié 2022), which is a dynamically adaptive multiscale wavelet-based code. WAVETRISK-OCEAN is an incompressible version of the atmosphere model WAVETRISK (Dubos and Kevlahan 2013; Aechtner et al. 2015; Kevlahan and Dubos 2019). WAVETRISK itself is based on the mimetic climate model DYNAMICO (Dubos et al. 2015). WAVETRISK uses a wavelet-based multiresolution grid structure, which permits arbitrary refinement of the local grid based on indicators of the relative approximation error (or other criteria). The discretization uses an icosahedral staggered C-grid approximation to spherical geometry.

WAVETRISK-OCEAN uses a Lagrangian vertical coordinate, which is highly accurate for ocean models. In general, the vertical grid must be remapped periodically to the initial grid or another target grid (e.g., isopycnal). However, in the two-layer cases considered here vertical remapping is not required, provided the vertical diffusion is sufficiently large to prevent layer collapse.

Vertical diffusion is approximated using a standard secondorder finite difference-finite volume discretization of Laplacian diffusion  $\partial_z(A_\nu\partial_z\mathbf{u})$ , where  $A_\nu$  is the vertical viscosity. The flux boundary conditions at the top and bottom layer interfaces are provided by the wind stress and bottom stress, respectively. The discrete approximations for vertical diffusion of velocity for the two-layer system are

$$\partial_t \mathbf{u}_1 = \dots - \frac{A_v}{h_1 h/2} (\mathbf{u}_1 - \mathbf{u}_2) + \frac{\boldsymbol{\tau}}{\rho_0 h_1}, \tag{11}$$

$$\partial_t \mathbf{u}_2 = \dots - \frac{A_v}{h_2 h/2} (\mathbf{u}_2 - \mathbf{u}_1) - r_b \frac{\mathbf{u}_2}{h_2}.$$
 (12)

The equivalent internal wave friction values in Eqs. (1) and (2) are therefore  $r_i = A_v/(h_ih/2)$ . The internal wave friction does not change the total linear momentum of the two-layer system  $\rho_0(h_1\mathbf{u}_1 + h_2\mathbf{u}_2)$ .

No-slip boundary conditions at coastlines are approximated using Brinkman volume penalization (Kevlahan et al. 2015). This method is derived from flow through a porous medium and controls the approximation error of the boundary condition by setting appropriately small values for the porosity and permeability in the solid regions. All cases considered here have uniform depth (i.e., no bathymetry features).

The multilayer ocean model uses barotropic-baroclinic mode time splitting via an implicit free surface to avoid the small time step imposed by the Courant-Friedrichs-Lewy (CFL) stability limit for the external mode. The method is stable for very large barotropic CFL numbers and accurate for barotropic CFL numbers of up to about 30. Implicit free

surface time splitting is commonly used ocean models and one popular example is the MITgcm model (Marshall et al. 1997).

The implicit free surface effectively damps the fast free surface wave motions and does not require an extremely accurate solution of the associated elliptic equation (unlike the rigid lid approach). We are interested in the slower geostrophic modes (i.e., turbulence) that determine the dynamics of WBCs. Since it has previously been found in the context of the shallow water model (Ford 1994) that this interaction is weak, we can safely damp the fast free surface waves. We have verified that the implicit free surface simulations give results for the vorticity field essentially identical to the non-time-splitting case run at the small barotropic time step  $\Delta t = 1.2x/\sqrt{gh}$ .

The combination of local grid adaptation and barotropic—baroclinic mode time splitting allows efficient numerical simulations at very high local resolution. In this paper we report results for a 1/6-scale Earth with finest grid size  $\Delta x_{\rm min} \approx 1.25$  km and coarsest grid size  $\Delta x_{\rm max} \approx 20$  km.

#### e. Spectral analysis

Investigation of turbulence dynamics requires accurate computation of energy spectra on the sphere. In addition, since we are particularly interested in turbulence generated by the WBC, we require local energy spectra associated with different regions of the boundary layer (e.g., equatorial and midlatitude).

The energy spectra are computed from saved vorticity data interpolated to the finest level of resolution  $\Delta x \approx 1.25$  km and then projected onto a uniform longitude-latitude grid of equivalent resolution. This means that we present energy spectra for the div-free, i.e., rotational, part of the velocity field. The curl-free, i.e., divergent, component is much weaker and is not relevant for the analysis of the geostrophic eddy dynamics we are interested in here. The spherical harmonics energy spectrum is then computed from the latitude-longitude data using the spherical harmonics toolbox SHTOOLS (Wieczorek and Meschede 2018).

In addition to global energy spectra, SHTOOLS can also compute the local energy spectrum corresponding to a specified spherical cap region of the sphere. This is done by "tapering": multiplying the data by suitable windowing functions and expanding the resulting field in spherical harmonics. Wieczorek and Meschede (2018) give details of the tapering process used to compute local energy spectra in specified regions, as well as an explanation of how to choose the various parameters. Our local spectra are computed with 6 tapers, an angular order of 2, and ensure that 99% of the total energy of the local energy spectrum is from the local region. The angular radius of the spherical cap localization domain is 20° (about 3% of the area of the sphere). We term the usual energy spectra computed over the entire sphere "global spectra" to distinguish them from the "local spectra" computed over subregions of the sphere.

#### f. Physical parameters

The basic physical parameters of our model are  $\Omega$  (the angular rotation rate), a (the radius of the sphere),  $r_b$  (bottom friction), wind stress magnitude  $\tau_0$ , lateral viscosity  $\nu$ , total depth H, mean layer depths  $H_1$  and  $H_2$ , and reduced gravity g'.

TABLE 2. Parameters for the simulations at three different rotation rates, where  $\Omega_E = 7.292\,11 \times 10^{-5}$  rad s<sup>-1</sup> is Earth's rotation rate and the reference latitude is 45°. All simulations use a 1/6-scale small Earth with radius  $a = a_E/6 = 1062$  km;  $U_{\rm wbc}$  is the observed maximum total velocity in the top layer,  $r_b$  is the bottom friction,  $A_v$  is the vertical viscosity,  $U_{\rm wbc}$  is the speed of the western boundary current,  $\delta_M$  is the Munk scale,  $\delta_S$  is the Stommel scale,  $\lambda_0$  is the external Rossby radius,  $\lambda_1$  is the internal Rossby radius,  $\delta_{\rm SM}$  is the submesoscale, and Ro is the Rossby number. The slow test case has the best resolution of the mesoscale and submesoscale, and hence of the baroclinic effects. The Munk–Stommel test case has a dominant baroclinic mode due to its much larger bottom friction and smaller vertical viscosity. The finest grid size is  $\Delta x \approx 1.25$  km.

| Test case    | $\Omega/\Omega_E$ | $r_b \text{ (m s}^{-1}\text{)}$ | $A_v  (\mathrm{m^2  s^{-1}})$ | $U_{\rm wbc}~({\rm m~s}^{-1})$ | $\delta_M$ (km) | $\delta_S$ (km)      | $\lambda_0$ (km) | $\lambda_1$ (km) | $\delta_{\rm SM}  ({\rm km})$ | Ro   |
|--------------|-------------------|---------------------------------|-------------------------------|--------------------------------|-----------------|----------------------|------------------|------------------|-------------------------------|------|
| Slow Munk    | 1/6               | $1.6 \times 10^{-8}$            | 4                             | 1.5                            | 3.1             | $2.5 \times 10^{-4}$ | 11 000           | 310              | 87                            | 23   |
| Normal Munk  | 1                 | $4.2 \times 10^{-8}$            | 4                             | 0.7                            | 1.7             | $1.7 \times 10^{-4}$ | 1920             | 52               | 3.2                           | 2.8  |
| Fast Munk    | 6                 | $1.4 \times 10^{-7}$            | 4                             | 0.1                            | 0.95            | $6.0 \times 10^{-5}$ | 320              | 8.6              | 0.043                         | 0.12 |
| Munk-Stommel | 1/6               | $4.0 \times 10^{-4}$            | $1.2 \times 10^{-4}$          | 3.5                            | 3.1             | 6.2                  | 11 000           | 310              | 203                           | 53   |

As was established by Stommel (1948), if bottom friction dominates the dynamics, the width of the WBC is the Stommel layer thickness,

$$\delta_S = \frac{r_b}{H\beta},\tag{13}$$

 $\beta = 2\Omega \cos(\phi)/a$  is the  $\beta$  parameter and  $\phi$  is the latitude. Note that, because we use spherical geometry,  $\delta_S$  is not constant.

Alternatively, if lateral viscosity  $\nu$  dominates the dynamics, then the width of the WBC is the Munk layer thickness (Munk 1950)

$$\delta_M = \left(\frac{\nu}{\beta}\right)^{1/3}$$
.

We set  $\nu$  to ensure that the Munk layer is reasonably well resolved and then set  $r_b$  to ensure that

$$\delta_M = 4H\delta_S,\tag{14}$$

so that lateral viscosity is the dominant effect as  $\Omega$  is varied. The vertical viscosity  $A_{\nu}$  is set just large enough to avoid layer collapse  $(4 \text{ m}^2 \text{ s}^{-1})$  and is similar in magnitude to the lateral viscosity  $\nu$ .

The mesoscale is estimated as the internal (i.e., baroclinic) Rossby radius of deformation,

$$\lambda_1 = \frac{c_1}{f_0},$$

where  $c_1=\sqrt{g'(H_1H_2)/H}$  is the speed of the baroclinic mode and  $f=2\Omega\sin\phi$  is the Coriolis parameter. We are particularly interested in small values of  $\Omega$  that ensure the mesoscale is large enough that the mesoscale motions are very well resolved. This means that the external (i.e., barotropic) Rossby radius  $\lambda_0=c_0/f$ , where  $c_0=\sqrt{gH}$  is the speed of external waves, is large and not of physical importance. Table 2 summarizes the physical parameters for each of the four test cases.

There are different ways to define the submesoscale length scale  $\delta_{\rm SM}$ . We have chosen to define it as the length scale where the local Rossby number Ro = 1 in the WBC, based on the velocity of the western boundary current observed in the simulation,  $U_{\rm wbc}$ , normalized by the local Coriolis parameter  $f_0$  at 45° (B. Fox-Kemper 2011, personal communication),

$$\delta_{\rm SM} = \frac{U_{\rm wbc}}{f_0}.$$

In the slow and normal rotation simulations  $\lambda_1/\delta_{SM}\approx 4$  and 14, respectively, and therefore there is a reasonable large gap between the two length scales (see Table 2).

The Rossby number

$$Ro = \frac{U_{\text{wbc}}}{\delta_M \Omega}.$$

Ro > 1 in our simulations (except for the fast test case). The local Rossby number (local relative vorticity divided by  $2\Omega$ ) in the vicinity of the WBCs is O(1), which suggests that submesoscale dynamics should be important there.

The model configuration and values of the physical parameters for our simulations our summarized in the following section.

#### g. Model configuration and test case parameters

We consider global simulations (i.e., spherical geometry) on a small 1/6-scale Earth. The small Earth and dynamically adaptive grid make very high resolutions feasible:  $\Delta x_{\rm min} \approx 1.25$  km for the results presented here. The gravitational acceleration  $g=9.806\,16$  m s $^{-2}$ , the reference density  $\rho_0=1028$  kg m $^{-3}$ , and the reference rotation rate  $\Omega_E=7.292\,11\times10^{-5}$  s $^{-1}$  (Earth value). The density difference between the two layers is  $\delta\rho=\rho_2-\rho_1=4$  kg m $^{-3}$ , or  $g'=0.038\,16$  m s $^{-2}$ . The total mean depth H=4 km in all cases and the mean layer depths are  $H_1=1$  km and  $H_2=3$  km in the two-layer simulations.

The top layer is forced by a latitude-dependent zonal wind stress

$$\tau_{u}(\phi) = -1.2 \,\tau_{0} \exp\left[-\left(\frac{|\phi| - 35^{\circ}}{20^{\circ}}\right)^{2}\right] \sin|6\phi| - \tau_{1} \exp\left[-\left(\frac{\phi}{10^{\circ}}\right)^{2}\right],\tag{15}$$

where  $\phi$  is the latitude in degrees, where  $\tau_0 = 0.4 \text{ N m}^{-2}$  is the maximum wind stress magnitude and  $\tau_1 = 5 \times 10^{-3} \text{ N m}^{-2}$ . This profile, shown in Fig. 1, is chosen to model the observed mean zonal wind stress (Ferreira et al. 2011). The meridional wind stress  $\tau_{\nu}$  is zero for all simulations. There are no external sources of buoyancy or mass. Wind stress acts only on the top layer, bottom friction acts only on the bottom layer, and internal drag acts only in the two-layer cases.

There is a single slab-like landmass with boundaries at latitudes  $-35^{\circ}$  and  $60^{\circ}$  and longitudes  $-15^{\circ}$  and  $15^{\circ}$  (see Fig. 2).

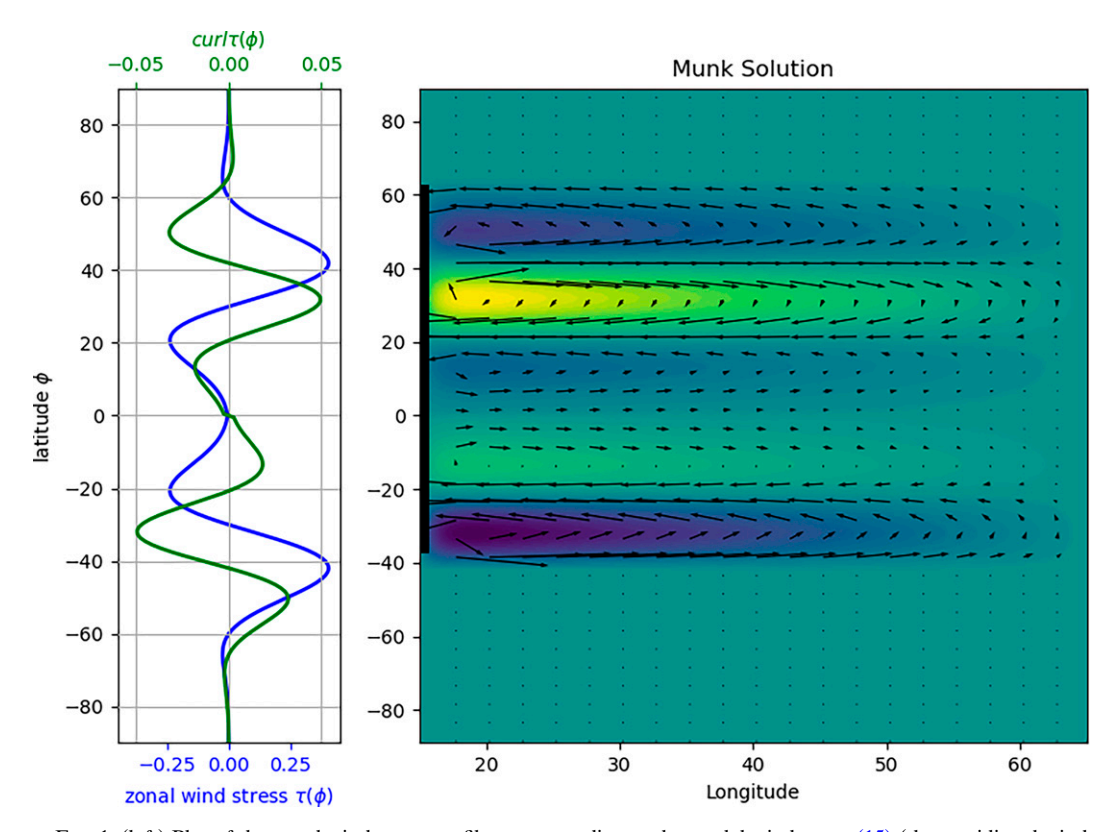


FIG. 1. (left) Plot of the zonal wind stress profile corresponding to the model wind stress (15) (the meridional wind stress is zero) (N m<sup>-2</sup>) and the curl of the wind stress as a function of latitude. (right) Plot of an idealization of the Munk solution for this particular wind stress. The Munk solution shows the expected location of the western boundary currents (WBC). The solid black line on the left denotes meridional extent of the continent. Latitude and longitude are in degrees.

This is the so-called "Drake Passage" test case (Ferreira et al. 2010) and is a good geometry for investigating turbulence generated by a western boundary current.

In all cases the initial conditions are zero displacement of the layer depths (i.e., zero initial displacement of the free surface and internal surface) and the ocean is at rest. All configurations use a flat bottom.

We investigate the sensitivity of turbulence dynamics and energy spectra to the rotation rate and the strength of the baroclinic mode. The four two-layer test cases and their associated physical parameters are summarized in Table 2. The first three all have a dominant Munk boundary layer, and hence are referred to as Munk layer cases. They differ mainly in their rotation rates. We focus on the slow rotation test case, since it has the best resolution of the submesoscale and mesoscale, but also present normal and fast rotation test cases for comparison. The slow test case exhibits the best-defined mesoscale eddy structure in all currents. The fourth case has Munk and Stommel boundary layers that are comparable in scale, and we therefore refer to it as a Munk–Stommel layer case.

We compare the slow Munk layer test case with a similar single layer test case with a total depth  $H=4\,\mathrm{km}$ . This allows us to directly compare the barotropic mode in the two-layer configuration with the (barotropic) solution of a similar one-layer configuration. It is not clear a priori how the baroclinic

mode modifies the barotropic mode in the two-layer case compared to the one-layer solution.

The three different Munk layer rotation cases all use very small bottom friction  $r_b = O(10^{-7}) \,\mathrm{m \ s^{-1}}$  to satisfy the relation (14) and a correspondingly large vertical viscosity  $A_v = 4 \,\mathrm{m^2 \ s^{-1}}$  to avoid layer collapse (Bleck et al. 2010; Kevlahan 2021). These values differ from the typical values of  $r_b = 4 \times 10^{-4} \,\mathrm{m \ s^{-1}}$  and  $A_v = 1.2 \times 10^{-4} \,\mathrm{m^2 \ s^{-1}}$  used in ocean models such as NEMO (Madec and NEMO Team 2016). The small bottom friction produces a relatively weak baroclinic mode (Rivière et al. 2004), containing only about 20% of the energy of barotropic mode at the submesoscale. We therefore complete our simulations with a "realistic" test case with a Munk–Stommel layer using the NEMO values for bottom friction and vertical viscosity. The test case produces a dominant baroclinic mode, with energy about 7 times that of the barotropic mode at the submesoscale.

#### 3. Vorticity diagnostics

In this section we present vorticity field results for the oneand two-layer global shallow water ocean models. We focus on qualitative descriptions of the vorticity fields, as this provides insights into the nature of the WBCs that develop, as well as the resulting eddying and turbulent fields. Barotropic

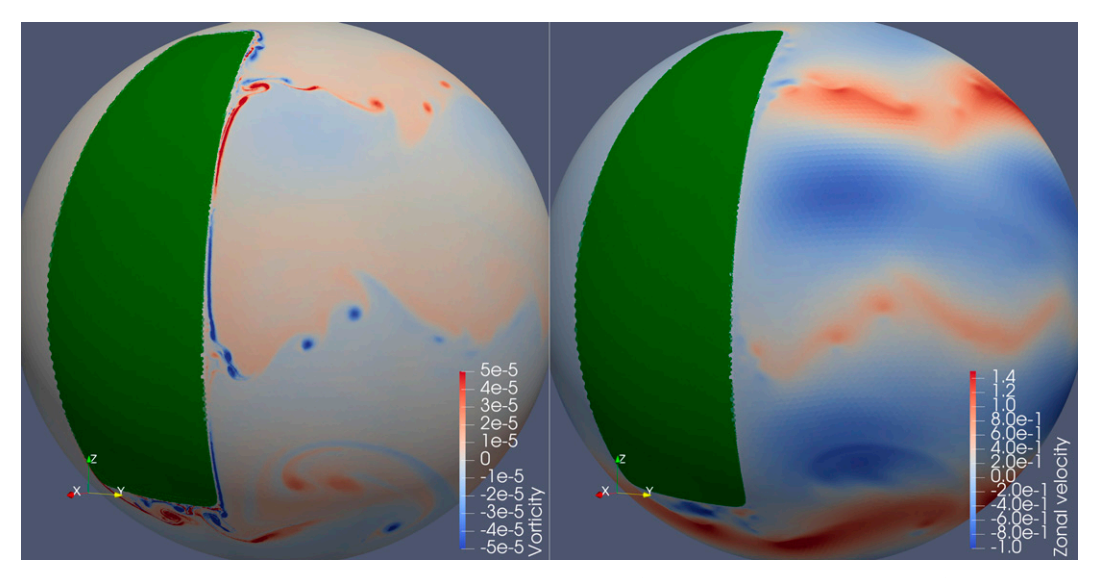


FIG. 2. One-layer simulation results at 450 days. (left) Vorticity (s<sup>-1</sup>) and (right) zonal velocity (m s<sup>-1</sup>) showing currents at midlatitudes, at the equator, and at the southern boundary of the landmass. The currents are characterized by intense eddy production and turbulence close to the western boundary of the ocean and southern solid boundaries. The eddies are then transported into the interior.

and baroclinic processes in the WBC generate eddies and turbulence. The dynamics of eddies and turbulence in the WBC and associate jets are the central themes of this paper.

All vorticity results are shown at 450 days when the currents and eddy structure are well developed and the simulations have reached an approximate statistical equilibrium. We use the term "eddies" for isolated coherent vortices and "turbulence" for complex regions of vorticity that include vortices of different sizes together with intense filamentary structures. The minimum grid size is  $\Delta x \approx 1.25$  km and the maximum grid size is  $\Delta x \approx 20$  km for all simulations. In section 4, we complement the physical space analysis with a discussion of the power law scaling of the energy spectra.

#### a. One-layer case and the basic gyre structure

We begin our discussion of the numerical simulations by making some qualitative observations about the vorticity and zonal velocity in the one layer (slow rotation Munk layer) simulation compared with multigyre structure predicted by the idealized Munk theory. This basic structure is maintained in the equivalent two-layer slow rotation Munk layer case.

The model simulations are initialized with the ocean at rest with constant zonal winds above, as shown in Fig. 1, which act to spin up the oceans. If there were no landmass, this configuration would be an "aquaplanet" simulation (e.g., Marshall et al. 2007) and the spinup of the ocean would not generate any WBC. In the aquaplanet scenario, the winds would drive the oceans and create mostly zonal currents, but not exactly since they would be deflected by the Coriolis force. However, in our case there is a landmass which strongly deflects the zonal flows and produces vorticity to generate meridional flow and subsequently WBC. This continent mimics the effect that the American continent has on the Atlantic Ocean.

Given the model wind stress in Fig. 1 (left) and Eq. (15), Munk's theory (Munk 1950) suggests that five gyres should form: three in the Northern Hemisphere and two in the Southern Hemisphere.

As predicted by theory, Fig. 2 shows that the imposed wind stress forcing generates three regions of strong mesoscale activity: at the equator and northern and southern subtropical gyres (Talley 2011). If we interpret our configuration as an idealized Atlantic Ocean, we observe analogs of the Gulf Stream (Stommel 2020) (in the northern midlatitudes) and the Brazilian Current (Dossa et al. 2021) (in the Southern Hemisphere). In the tropics we reproduce the Equatorial Current (Philander 2001).

Because the mesoscale is very well resolved in this slow rotation simulation, Fig. 2 (left) shows intense eddy generation and transport into the interior of the gyres. Turbulent regions form at the southern boundary of the continent and at the northern midlatitude current near the coast. Since the Coriolis force vanishes at the equator, the motion is much less balanced in the tropics and therefore the barotropic dynamics is significantly different compared to the midlatitudes.

It is clear from these results that single layer (barotropic) dynamics can produce WBCs with strong eddy and turbulence generation. In the following section we compare the one-layer results with a similar two-layer simulation which includes a single baroclinic mode.

## b. Comparison of one- and two-layer slow rotation Munk layer simulations

The baroclinic field (Fig. 3, right) is a new feature of the two-layer simulation that is absent in the one-layer simulation. Comparing the one- and two-layer simulation is therefore a clean way of understanding the additional dynamics

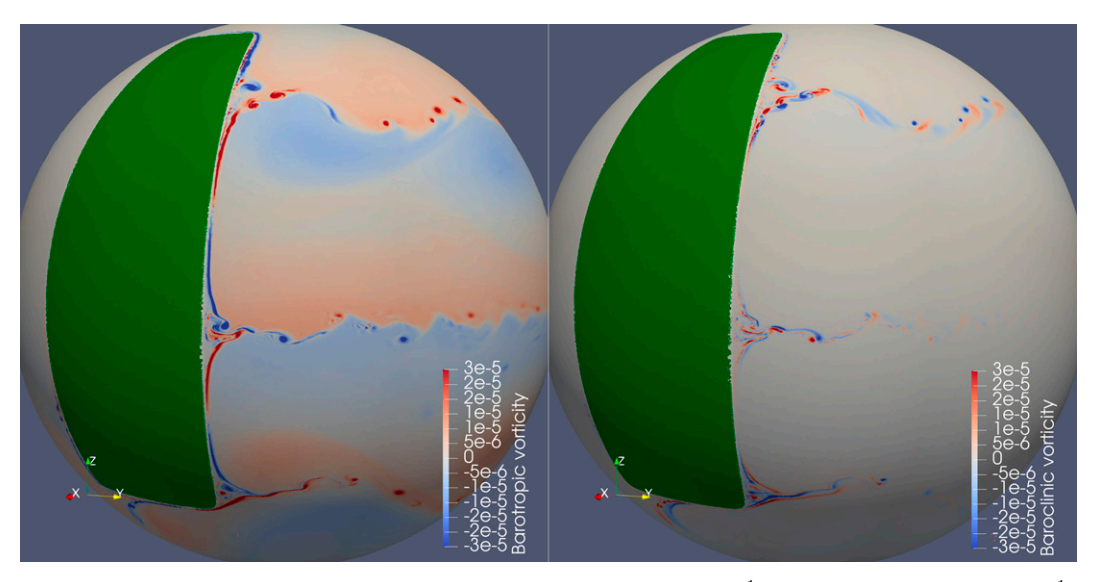


Fig. 3. Two-layer slow rotation simulation at 450 days. (left) Barotropic vorticity ( $s^{-1}$ ) and (right) baroclinic vorticity ( $s^{-1}$ ) in the top layer.

introduced by the first baroclinic mode. We note that this mode can produce both balanced and unbalanced motions.

The barotropic part of the two-layer vorticity fields in Fig. 3 (left) is qualitatively similar to the one-layer vorticity (barotropic) in Fig. 2 (left). The locations of the bands of vorticity coincide and the magnitudes of the velocity and vorticity are similar. Both vorticity fields are dominated by eddies (i.e., coherent vortices) that are transported into the ocean interior. However, there are some interesting differences.

All barotropic currents meander over a broader area in the one-layer case. There is also more turbulence near the western boundary at the equator in the two-layer case, but much less turbulence at the southern solid boundary. This is presumably because the continent does not extend as far south as it does north. The turbulent region associated with the southern subtropical WBC is shifted to the eastern boundary of the continent, just north of the corner. More significantly, there is a pronounced boundary layer on the western boundary of the continent in the Southern Hemisphere (although this not highlighted in the standard view shown in the figures). This boundary layer is almost entirely absent in the one-layer simulation and has vorticity of the opposite sign.

The baroclinic vorticity is qualitatively different from the barotropic vorticity, although their magnitudes are similar. The baroclinic vorticity has much stronger gradients and a more filamentary turbulent structure. This is not surprising since the internal Rossby radius is narrower than the external Rossby radius. Most significantly, the baroclinic vorticity has additional eddies of both signs compared with the barotropic field. These qualitative differences are due to the baroclinic vorticity generation that is only possible in the two-layer case. The results shown in section 4 reveal that this difference is reflected in a shallower -5/3 power law energy spectrum for the baroclinic field compared to the -3 power law energy spectrum of the barotropic field.

The baroclinic vorticity structure is important as it signifies that energy is being transferred from the horizontal to the vertical, and this generates potential energy in the basic state. Furthermore, baroclinic vorticity production is active, even though the two-layer case adds only a single baroclinic mode (i.e., the vertical motion of the internal free surface).

Studying the same physical problem with more vertical layers could determine whether this process contributes to the MOC (Marshall et al. 1997), but such a study is beyond the scope of this paper. Our two-layer model does not allow for the sinking of dense water or the rising of light water so it cannot address those aspects of the MOC. However, it can describe the horizontal transport either at the surface or at depth.

## c. Vorticity structure: Effect of rotation rate

As shown in Table 2, the main effect of increasing the rotation rate in the normal and fast rotation cases is to decrease the mesoscale  $\lambda_1$  and the submesoscale  $\delta_{SM}$ . This, in turn, significantly decreases the resolution of the turbulent mesoscale dynamics. These scales are well resolved in the slow rotation Munk layer case: the mesoscale with 248 grid points and the submesoscale with 70 grid points. However, in the normal rotation case they are resolved with only 42 and 3 grid points, respectively. In the fast rotation case, the mesoscale resolved with only 7 grid points and the submesoscale is not resolved at all. The Rossby number is also proportionally smaller for the faster rotation cases. These differences lead to clear qualitative differences in the corresponding barotropic and baroclinic vorticity fields.

Figure 4 shows the vorticity for the normal rotation Munk layer case. The three currents are strikingly different in the normal rotation case compared with the slow rotation case. The currents are all far more turbulent and mostly lack the well-defined isolated eddies that characterize the slow rotation

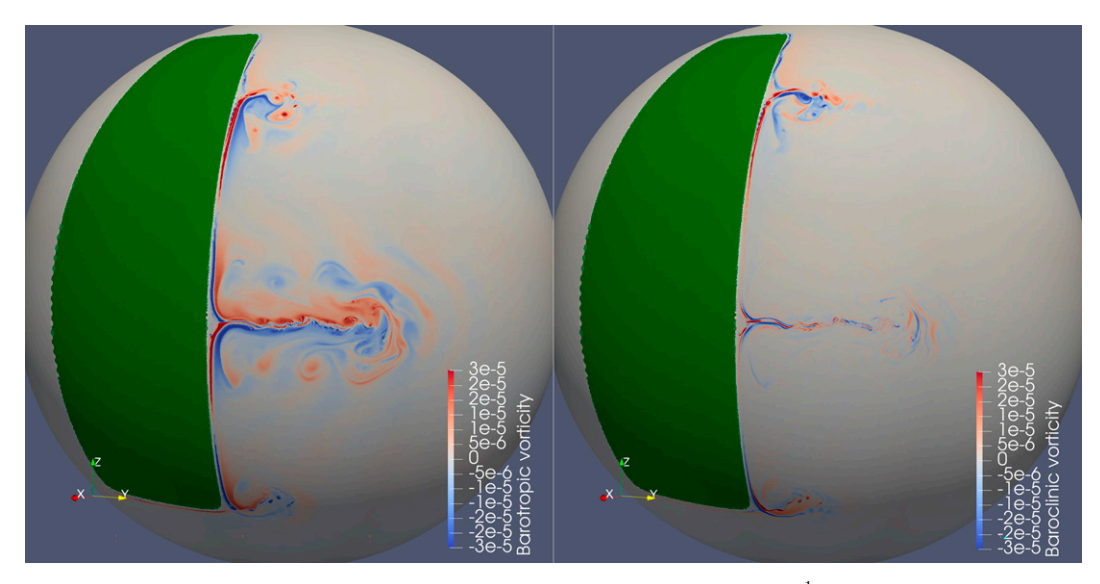


Fig. 4. Two-layer normal rotation simulation at 450 days. (left) Barotropic vorticity ( $s^{-1}$ ) and (right) baroclinic vorticity ( $s^{-1}$ ) in the top layer.

case. In addition, the subtropical currents in the north and south do not extend very far into the midocean (i.e., the jet is less energetic). The equatorial current has a striking turbulent jet structure and is the strongest of the three in the normal rotation case. These subtropical and equatorial jets are compared in detail in the following section. In contrast to the slow rotation case, there is no eddy activity at the southern boundary of the continent. A case of reduced rotation was run (not shown here) and it gave rise to much less vortex shedding as a result of the jet being wider and therefore more stable.

Clearly, a slower rotation rate inhibits the formation of eddies and favors the development of turbulence and eddy transport into the interior has been reduced. Figure 5 shows the vorticity for the fast rotation Munk layer case. The unresolved submesoscale and the much smaller Rossby number have completely eliminated the three currents in the fast rotation case. Isolated eddies are unable to form, and the vorticity is primarily filamentary. Intense vorticity is limited to a narrow band close to the western boundary. The baroclinic vorticity is simply the barotropic vorticity with the sign reversed.

These results show that changing the rotation rate fundamentally modifies the WBC and the vorticity structure and dynamics. Slow rotation favors the formation of isolated eddies, while normal rotation favors the formation of turbulence. In the fast rotation simulation, where the submesoscale

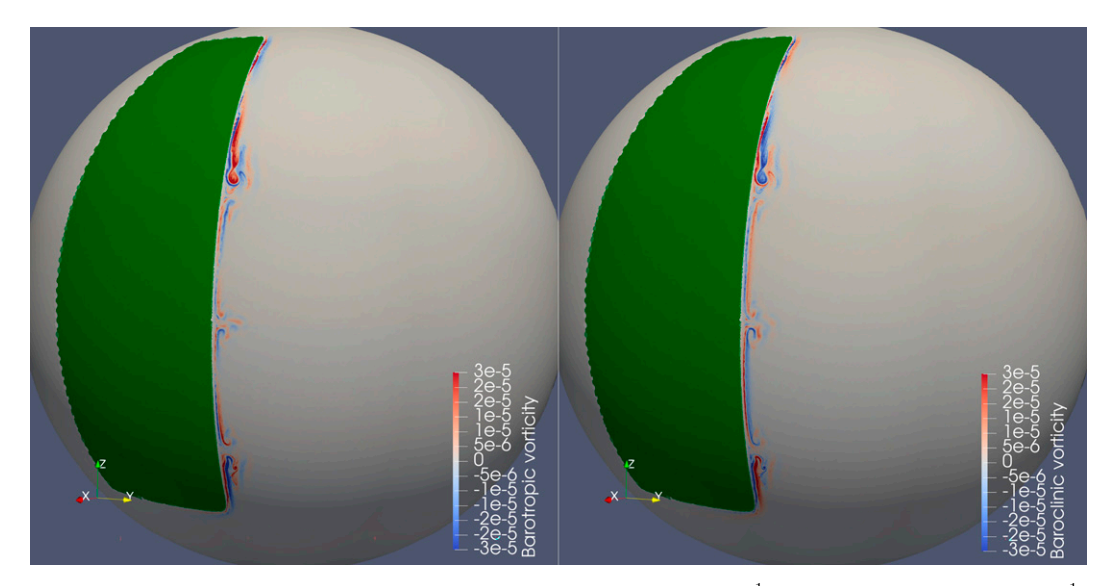


FIG. 5. Two-layer fast rotation simulation at 450 days. (left) Barotropic vorticity (s<sup>-1</sup>) and (right) baroclinic vorticity (s<sup>-1</sup>) in the top layer.

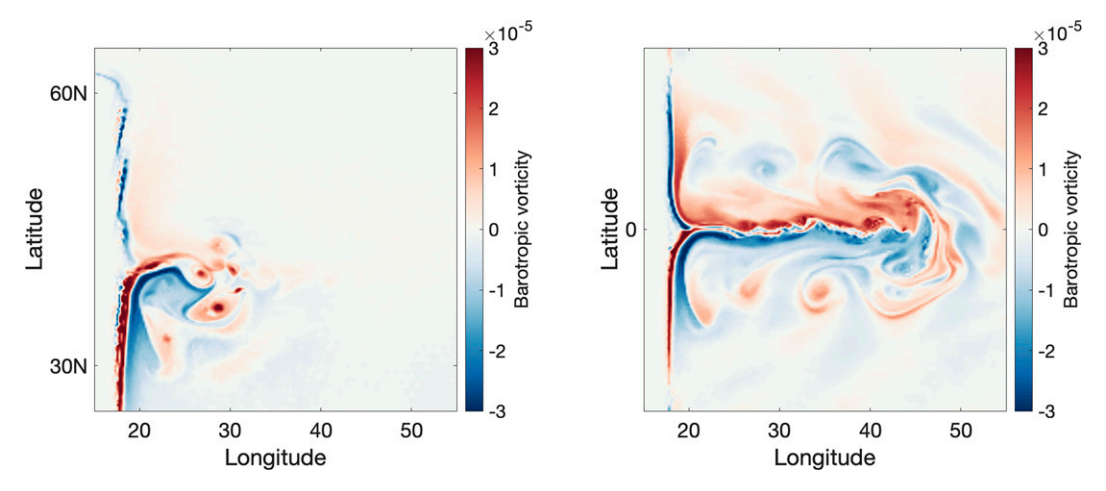


FIG. 6. Local barotropic vorticity (left) in the Northern Hemisphere and (right) at the equator in the normal rotation case. Latitude and longitude are in degrees. The equatorial jet is more turbulent, while the midlatitude jet has more clearly defined eddies. This figure shows the regions that are used for computing local spectra in section 4d.

is not resolved, the eddies and turbulence both disappear. These differences are likely due to the fact that the dynamics are not sufficiently well resolved in the fast rotation case.

## d. Equatorial current compared to midlatitude current in the normal rotation test case

In Fig. 6 we compare in detail the local barotropic vorticity in the Northern Hemisphere and at the equator in the normal rotation case. The dynamics of these two meandering currents are quite different. The midlatitude current shown in Fig. 6 (left) is turbulent, remains close to the boundary, and has some well-defined eddies. In contrast, the equatorial current shown in Fig. 6 (right) strongly resembles a turbulent jet, with less intense vortices and much greater penetration into the interior of the ocean. The zonal velocity of the equatorial current is 40% stronger than that of the midlatitude current: 0.7 m s<sup>-1</sup> compared to 0.5 m s<sup>-1</sup>.

While the midlatitude current is in near-geostrophic balance, this is not the case at the equator since the Coriolis force is close to zero. We suspect that this fundamental difference in physics is what leads to a much more turbulent current at the equator, as it is well known that more types of instabilities can occur in unbalanced motions (Molemaker et al. 2005), e.g., the inertial instability. Even though the Rossby number is about 8 times smaller in this case than in the previous slow rotation case, the WBCs are much more turbulent.

In section 4d we use local spectra to investigate whether these qualitative differences lead to differences in their respective barotropic and baroclinic energy spectra.

#### e. Munk-Stommel boundary layers

The previous simulations all use relatively small bottom friction and large vertical viscosity compared with the values used in ocean models. The small bottom friction leads to a relatively weak baroclinic mode (Rivière et al. 2004) with about 20% of the energy of the barotropic mode at the submesoscale.

In this section we present results for the Munk–Stommel test case where larger bottom drag and smaller vertical diffusion (see Table 2) produce a dominant baroclinic mode. Note that the much larger bottom friction produces a correspondingly larger Stommel thickness,  $\delta_s = 6.2$  km. This is equal to the Munk layer thickness, which is unchanged. In contrast to the other test cases, vertical diffusion of momentum is much stronger.

Figure 7 confirms that increasing the bottom friction and decreasing the vertical viscosity produces a dominant baroclinic mode. In the next section we will see that the baroclinic mode is about 7 times stronger than the barotropic mode at the submesoscale. Although the vorticity is still dominated by mesoscale eddies, they are now scattered over the entire sphere and do not form clearly defined currents. There is much less filamentary turbulence compared to the equivalent (slow rotation) small bottom friction case. The midlatitude current has shifted sharply northward and the strong equatorial current present in Fig. 3 has vanished entirely.

#### 4. Energy spectra diagnostics

The vorticity fields discussed in the previous section give a good qualitative picture of where eddies are generated and which WBCs are most turbulent. They also reveal the effects of rotation rate and resolution of the mesoscale and submesoscale on barotropic and baroclinic vorticity production and transport.

However, a more precise and quantitative understanding of eddy and turbulence structure is given by energy spectra. In particular, fully developed turbulence is characterized by the presence of one or more scale-free inertial ranges with a power law scaling in each inertial range. Different turbulent regimes (2D, 3D, QG, SQG, etc.) are characterized by different energy spectra and power laws.

Our goal in this section is to compare the inertial range scaling of the barotropic and baroclinic modes for the

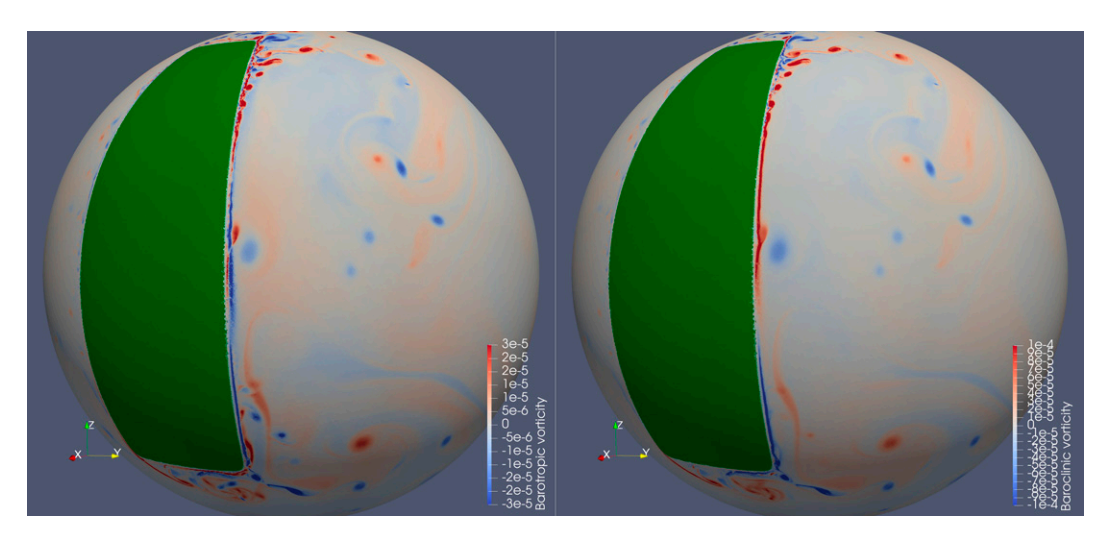


FIG. 7. Two-layer slow rotation simulation with Munk–Stommel bottom friction and vertical viscosity at 450 days. (left) Barotropic vorticity and (right) baroclinic vorticity in the top layer. We use different scales for the barotropic and baroclinic vorticity because the baroclinic vorticity is about 3 times stronger than in the other test cases. Note the very different eddy structure compared to the equivalent small bottom friction and large vertical diffusion case shown in Fig. 3.

configurations discussed in section 3. We are particularly interested in using the energy spectra to characterize the eddy or turbulence vorticity structures generated in each case.

We plot the energy spectra in terms of the spherical harmonic wavelength  $\lambda$ , i.e., the equivalent wavelength on the sphere based on the Jeans relation  $\lambda = 2\pi a/\sqrt{l(l+1)}$ , where l is the degree of the spherical harmonic and a is the radius of the sphere. The wavenumber  $k=1/\lambda$ , which is the inverted horizontal axis used in the energy spectra figures makes it is easy to identify the length scales while preserving the usual presentation of energy spectra in terms of wavenumber.

Different regions of the WBC may have different energy spectra because of their different vorticity structure and local conditions (e.g., strength of Coriolis force). To investigate how the energy spectra vary locally, we use SHTOOLS to compute local energy spectra in selected spherical cap regions (e.g., midlatitude or equatorial jets), as explained in section 2e.

All spectra presented are averages of 10 spectra computed for the top layer at 5-day intervals from 405 to 450 days. We checked that the averaged spectra are indeed stationary by modifying the window over which we take the average. In fact, the slopes do not change if we compare spectra of single times to the average: they are just noisier.

# a. One- and two-layer slow rotation Munk layer energy spectra

In Fig. 8 we plot the global energy spectra for the one-layer (left), barotropic component of the two-layer simulation (center), and the baroclinic component of the two-layer simulation (right). The inertial range is approximately the planetary scale since that is the scale of the forcing by the wind stress. It is about twice as large as  $\lambda_1$ .

For intermediate wavenumbers, we see that both the onelayer and two-layer barotropic spectra have power laws of -3.

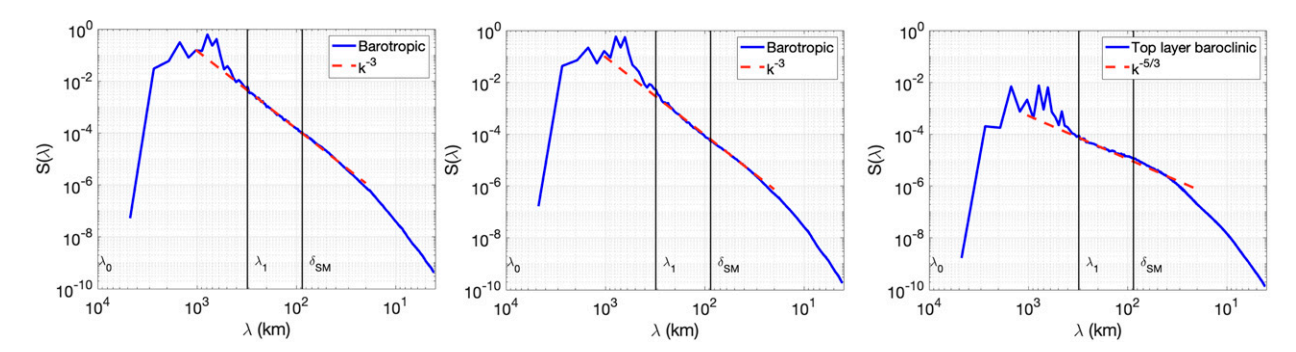
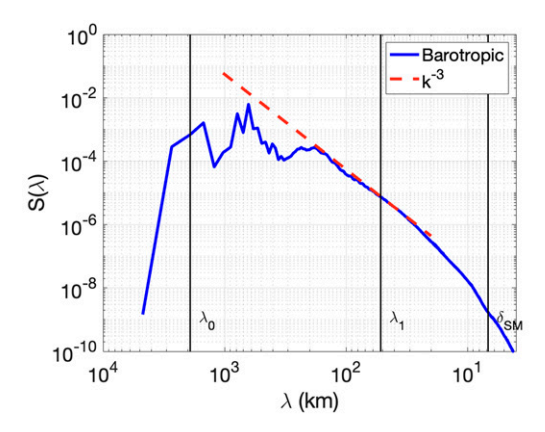


FIG. 8. Global spherical harmonic energy spectra of the slow rotation case. The term  $\lambda$  is the wavelength and  $k = 1/\lambda$  is the wavenumber;  $\lambda_0$  and  $\lambda_1$  are the external and internal deformation radii, respectively, and  $\delta_{\rm SM}$  is the submesoscale. (left) One-layer and (center) two-layer barotropic. (right) Two-layer baroclinic. The baroclinic mode has about 20% of the energy of the barotropic mode at the submesoscale. The energy spectrum of the total velocity field also has a power law scaling of -3.



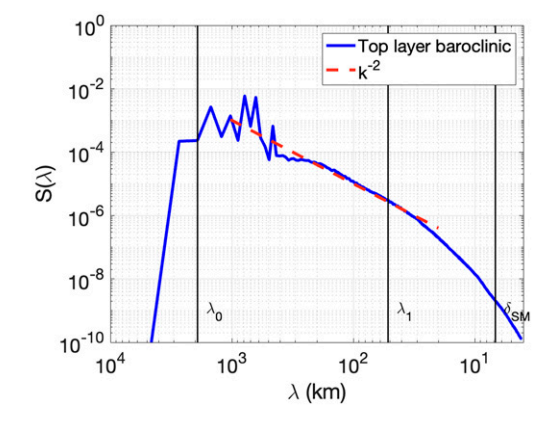


FIG. 9. Global spherical harmonic energy spectra of the two-layer normal rotation case. The term  $\lambda$  is the wavelength and  $k=1/\lambda$  is the wavenumber;  $\lambda_0$  and  $\lambda_1$  are the external and internal deformation radii, respectively, and  $\delta_{\rm SM}$  is the submesoscale. (left) Barotropic energy spectrum. (right) Baroclinic energy spectrum. The power law of the baroclinic spectrum is slightly steeper than in the slow rotation case: -2 compared to -5/3.

This slope is consistent with a forward enstrophy cascade, which is what is typically observed when studying turbulent flows in the QG model away from the boundaries (Salmon 1998).

In contrast, the baroclinic spectrum is characterized by an inertial range with much shallower slope, with a power law close to -5/3, as for the inverse energy cascade in two-dimensional turbulence. However, this slope has also been found in studies of surface quasigeostrophic (SQG) turbulence, which models the flows near the surface of the ocean (Sukhatme and Pierrehumbert 2002; Lapeyre 2017; Perruche et al. 2011).

It is interesting that we observe slopes of both -3 and -5/3 in the same model, but in two different fields (barotropic and baroclinic). For SQG, Tulloch and Smith (2009) find a -3 energy spectrum power law associated with an inverse two-dimensional cascade of barotropic energy and a -5/3 energy spectrum power law associated with a forward three-dimensional cascade of buoyancy variance (see Table 1). It is also noteworthy that a single baroclinic mode is sufficient to produce the -5/3 scaling.

However, it should be noted that at the submesoscale the baroclinic field is about 5 times weaker than the barotropic field, and therefore the energy spectrum of the total field is dominated by the barotropic dynamics and has a slope of -3.

Notice that in all the energy spectra shown in Fig. 8, the -3 or -5/3 inertial range ends at about 20 km. This length scale is not significantly affected by rotation and is much smaller than the external and internal radii of deformation.

## b. Normal and fast rotation Munk layer energy spectra

Figure 9 shows the barotropic and baroclinic energy spectra for the normal rotation test case. The results are broadly similar to the slow rotation case, but with a smaller power law range and a slightly steeper -2 power law for the baroclinic energy spectrum (still typical of observed and modeled three-dimensional ocean flow, see Table 1). The smaller inertial ranges are likely due to the less-well-resolved mesoscale and submesoscale.

Figure 10 shows the barotropic and baroclinic energy spectra for the fast rotation test case. The results are qualitatively different from the slow and normal rotation cases and illustrate how the distinct vorticity dynamics of the fast case shown in the previous section affect the energy spectrum. There is a flat power law region at intermediate scales and a steep and well-defined -4 or -3.5 power law at small scales. These qualitatively different results are likely due to the fact that the submesoscale is completely unresolved in this case. Indeed, Morvan et al. (2020) find that a -4 slope is associated with dominant mesoscale eddy dynamics, while a -2 slope is associated with dominant submesoscale dynamics. The flat power law may not be significant, although a similar energy spectrum has been observed in the ocean (see Table 1).

#### c. Munk-Stommel layer test case energy spectra

Figure 11 shows the barotropic and baroclinic energy spectra for the realistic (Munk–Stommel layer) test case. The baroclinic mode strongly dominates in this case, with about 7 times the energy of the barotropic mode at the submesoscale. Both spectra have power laws of -3. It seems that the baroclinic mode has extracted energy from the barotropic mode, leading both spectra to converge to a -3 power law. Since the -3 spectrum is typical of one-layer two-dimensional dynamics, the -5/3 or -2 scaling observed with small bottom friction may be due to the baroclinic mode being weakly coupled to the barotropic mode in those cases. The absence of a distinct -5/3 power law suggests there is no longer a forward baroclinic energy cascade in this case.

### d. Local spectra at midlatitude and equator

One of strengths of the SHTOOLS spherical harmonics toolbox is that it can compute spectra over localized regions, and thus we can analyze the contributions to the global spectra from specific currents (e.g., midlatitude and equatorial). Fourier analysis tells us that in a signal containing regions of different regularity the global energy spectrum is set by the most singular region (i.e., the one with the shallowest power

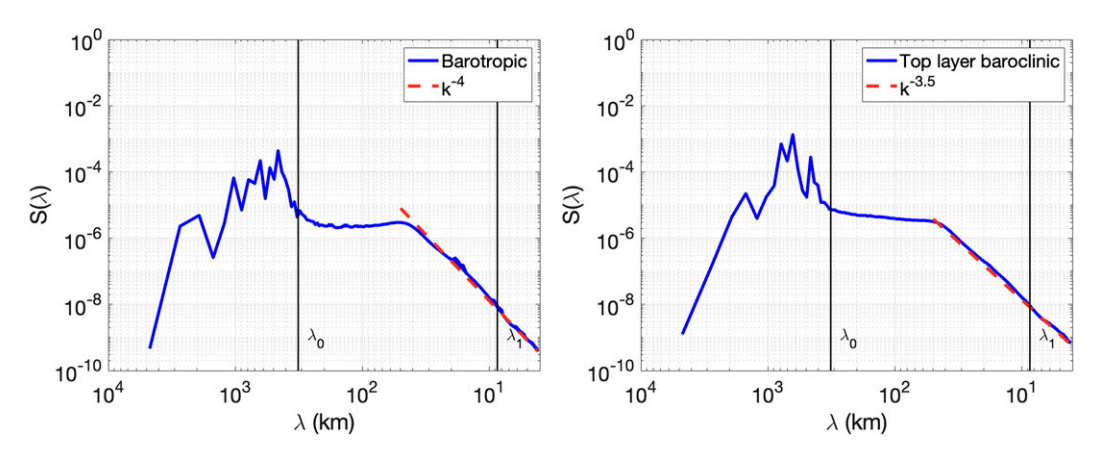


FIG. 10. Global spherical harmonic energy spectra of the two-layer fast rotation case. The term  $\lambda$  is the wavelength and  $k = 1/\lambda$  is the wavenumber;  $\lambda_0$  and  $\lambda_1$  are the external and internal deformation radii, respectively (the submeso-scale is not resolved in this case). (left) Barotropic energy spectrum. (right) Baroclinic energy spectrum. The unresolved submesoscale leads to a very different spectrum, with a flat energy spectrum at intermediate scales and power laws steeper than -3 at small scales for both modes.

law spectrum). We therefore expect that some regions of the WBC could have local energy spectra with power law slopes steeper than that of the global energy spectrum.

We focus here on comparing the local spectra in the subtropical and equatorial currents shown in Fig. 6) with the global spectra in Fig. 9. We picked this case since the vorticity structure in the two currents is distinct: eddies at midlatitude and turbulent jet at the equator. The vortical parts of the currents are also more localized than in the slow rotation case, making local analysis feasible. Both the midlatitude and equatorial local regions are spherical caps with angular radius of 20°.

Figure 12 shows the local energy spectra for the midlatitude and equatorial regions shown in Fig. 6. The barotropic power law of the local energy spectrum for the midlatitude current is about -3, while that of the equatorial jet is steeper: -4. This

suggests that the -3 power law of the barotropic global spectrum is set by the midlatitude current.

In contrast, the -5/3 power law of the local baroclinic energy spectrum of the equatorial turbulent jet is shallower than the -2.5 power law of the midlatitude eddy. This suggests that it is possible that the equatorial jet that determines the global power law, which is close to -2. These results also suggest that the Coriolis force has the effect of steepening the baroclinic spectrum, increasing its power law from -5/3 to -2.5. If the long internal wave turbulence analysis of Lvov and Tabak (2001) is valid, this could suggest that wave turbulence is more active at midlatitudes.

These local energy spectrum results are perhaps not surprising given the more turbulent structure of the equatorial turbulent jet (more like forced turbulence) and the eddy

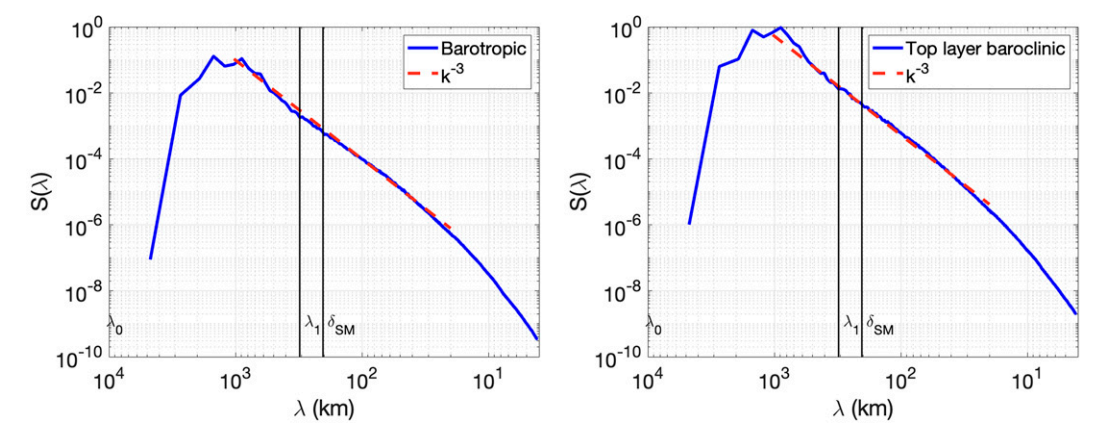


FIG. 11. Global spherical harmonic energy spectra of the Munk–Stommel layer case. The term  $\lambda$  is the wavelength and  $k = 1/\lambda$  is the wavenumber;  $\lambda_0$  and  $\lambda_1$  are the external and internal deformation radii, respectively, and  $\delta_{SM}$  is the submesoscale. (left) Barotropic energy spectrum. (right) Baroclinic energy spectrum. The baroclinic mode dominates in this case, with about 7 times the energy of the barotropic mode at the submesoscale, and both spectra have power laws of -3.

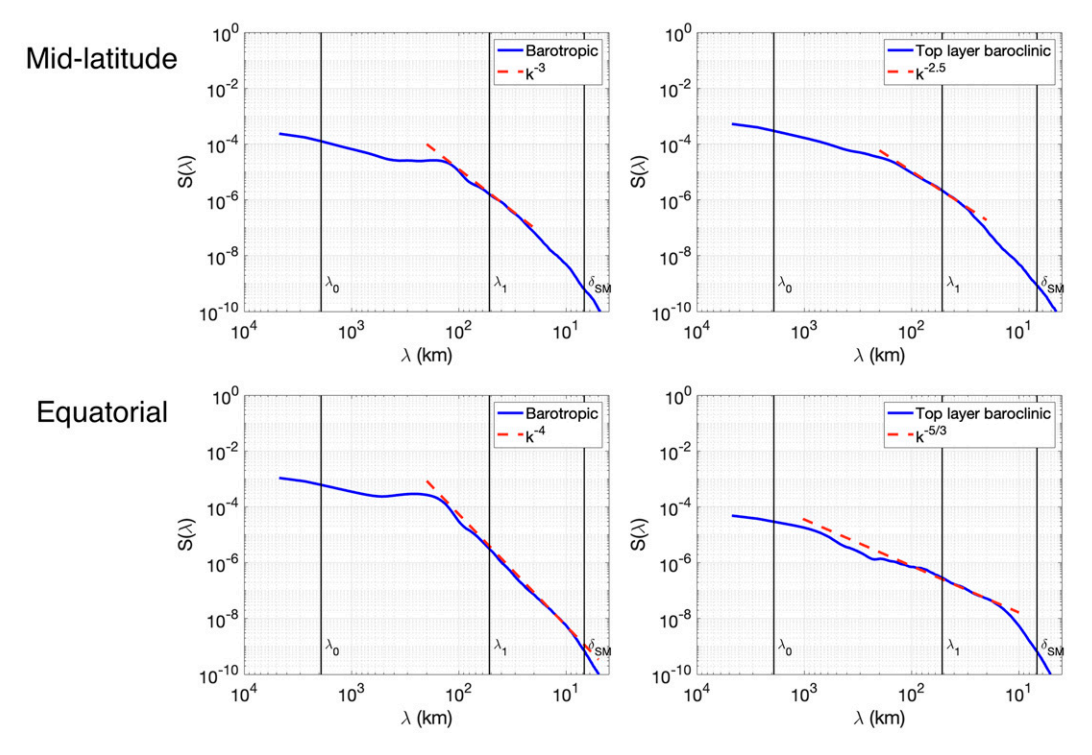


FIG. 12. Local spherical harmonic energy spectra for two-layer normal rotation case in the midlatitude and equatorial regions shown in Fig. 6. The terms  $\lambda_0$  and  $\lambda_1$  are the external and internal deformation radii, respectively;  $\delta_{SM}$  is the submesoscale. (top) The midlatitude region centered at (45°N, 35°E) with an angular radius of 20°. (bottom) The equatorial region centered at (0°N, 35°E) with an angular radius of 20°. Note that there is much less energy in these local regions than for global energy spectra integrated over the entire sphere.

dominated structure of the subtropical WBC midlatitude current (more similar to decaying two-dimensional turbulence).

#### 5. Conclusions

We have used the global dynamically adaptive WAVETRISK-OCEAN code to compare the properties of barotropic and single-mode baroclinic turbulence in a two-layer shallow water ocean model. The base configuration uses a 1/6-scale "small" Earth with layer depths  $H_1 = 1$  km,  $H_2 = 3$  km, and density difference  $\delta \rho = \rho_2 - \rho_1 = 4$  kg m<sup>-3</sup>. The maximum magnitude of the wind stress is  $\tau_0 = 0.4$  N m<sup>-2</sup>. We compare results for simulations with a dominant Munk boundary layer at different rotation

rates with one that has Munk and Stommel layers of essentially the same size.

The power law scaling for the various configurations is summarized in Table 3. The result for the power law of the barotropic component is robust: it is -3 for all one- and two-layer configurations. The most interesting result is that the energy spectrum power law of the single baroclinic mode is between -5/3 and -2 for all small bottom friction cases that resolve the submesoscale. These results are similar to Tulloch and Smith's (2009) theory for SQG turbulence, who find a -3 energy spectrum power law associated with an inverse two-dimensional cascade of barotropic energy and a -5/3 energy spectrum power law associated with a forward three-

TABLE 3. Global energy spectrum results. Note that the submesoscale is not resolved in the fast rotation case and the baroclinic energy dominates in the large bottom friction case. These results are the same for the top and bottom layers. Full details of the parameters for each test case are given in Table 2.

| Test case                | Component                 | Power law $p$ , $E(k) \propto k^p$ |  |
|--------------------------|---------------------------|------------------------------------|--|
| One layer, slow rotation | Barotropic                | -3                                 |  |
| Slow and normal rotation | Barotropic                | -3                                 |  |
| Fast rotation            | Barotropic                | -4                                 |  |
| Slow rotation            | Baroclinic                | -5/3                               |  |
| Normal rotation          | Baroclinic                | -2.5                               |  |
| Fast rotation            | Baroclinic                | -3.5                               |  |
| Large bottom friction    | Barotropic and baroclinic | -3                                 |  |

dimensional cascade of buoyancy variance (see Table 1). The shallow slope of the baroclinic mode is similar to what is observed in oceanic turbulence, and this suggests that the first baroclinic mode could play an important role in producing the slopes that are observed.

In the fast rotation Munk layer case, where the submesoscale is not resolved, the barotropic and baroclinic energy spectra have steeper slopes of approximately -4 and -3.5, respectively. This is consistent with the observations of Morvan et al. (2020), who find that a -4 power law is associated with dominant mesoscale motions, while a shallower -2 power law is associated with an active submesoscale.

However, in the two-layer case with a dominant Munk layer, the baroclinic mode only has about 20% of the energy of the barotropic mode and therefore the spectrum of the power law of the total kinetic energy spectrum is −3. We also ran a simulation with Munk and Stommel layers of comparable sizes and this case produced a baroclinic mode with 7 times the energy of the barotropic mode. However, the power law of both the baroclinic and barotropic modes is −3 in this case. This is in contrast to the SQG results of Tulloch and Smith (2009), which suggests that only the two-dimensional barotropic cascade is active in this case. This Munk–Stommel layer case did not produce an equatorial jet, which is unrealistic.

The local energy spectra results in Fig. 12 confirmed that the global energy spectra are indeed controlled by the vorticity in the WBC. Comparing local spectra in the midlatitude and equatorial regions for the normal rotation case suggests that the Coriolis effect steepens the spectrum slightly: changing it from -5/3 to -2.5. It is interesting that the long internal wave turbulence analysis of Lvov and Tabak (2001) predicts a -2.5 power law.

Salmon's (1998) model of two-layer geostrophic turbulence forces the system by adding energy to the baroclinic mode at large scales, which then cascades to smaller scales. The baroclinic energy is converted to barotropic energy at the internal Rossby radius of deformation and, subsequently, the barotropic energy cascades to both larger and smaller scales. This is consistent with what we find and also what is found by Tulloch and Smith (2009), since there appears to be both an inverse cascade of barotropic energy at the large scales and a direct cascade of baroclinic energy at the small scales. Since the Munk layer cases can produce shallow energy spectra of -5/3, they must be generating submesoscale dynamics. In contrast, the Munk-Stommel case has energy spectra with a much steeper slope and therefore does not generate submesoscale dynamics. We attribute the differences between these two results to the fact that the bottom boundary layer is in the form of a Rayleigh drag, and therefore dissipates all length scales equally. This seems to prevent the generation of submesoscale dynamics in the large bottom friction Munk-Stommel layer case.

No configuration produced a dual cascade with two well-defined power laws, like the -3 and -5/3 combination predicted by QG or SQG. However, since we found that the bar-otropic component has a power law of -3 and the baroclinic component has a power law of about -5/3 it is possible that adding more vertical layers (i.e., more baroclinic modes) may amplify the first baroclinic mode by allowing transfer of

energy from the higher-order baroclinic modes to produce a dual power-law energy spectrum. Such a mechanism has been proposed by Fu and Flierl (1980). In other words, we have the ingredients to produce either the (-5/3, -3) QG or (-3, -5/3) SQG spectra, depending on the relative amounts of energy in the barotropic and baroclinic modes at each wavenumber. This conjecture is a subject for future investigation.

Focusing on the simple case of two-layer shallow water turbulence has revealed that a fundamental characteristic of submesoscale turbulence can be captured by the first baroclinic mode. Two-layer models can be used to help understand the transfer of energy in the global ocean by allowing extremely high-resolution simulations that are impractical with realistic three-dimensional models that typically contain 60 or 80 layers.

Future research, comparing two-layer and multilayer models, will help us further understand the effect of adding more baroclinic modes: Which important turbulence physics is absent in a two-layer model? Which physics is simply masked by the much stronger barotropic mode? Since WAVETRISK-OCEAN (Kevlahan and Lemarié 2022) is a multilayer ocean model that allows inhomogeneous density layers, we can continue to use it to investigate turbulent energy cascades in more realistic scenarios.

Acknowledgments. The authors acknowledge their NSERC Discovery Grants and a grant of computer time from Compute Ontario (computeontario.ca) and Compute Canada (www.computecanada.ca). We thank Baylor Fox-Kemper for his helpful discussions and comments on the physics of turbulent wind-driven gyres.

Data availability statement. The WAVETRISK-2.1 compute code used to generate the results presented here is published under the Creative Commons License 4.0 as https://doi.org/10.5281/zenodo.5608548. The raw data that was used to produce the figures in this paper are very large (14 GB). They are on long-term storage on the Compute Canada machine Niagara and are available from the corresponding author on request.

#### REFERENCES

Aechtner, M., N. K.-R. Kevlahan, and T. Dubos, 2015: A conservative adaptive wavelet method for the shallow water equations on the sphere. *Quart. J. Roy. Meteor. Soc.*, 141, 1712–1726, https://doi.org/10.1002/qj.2473.

Afanasyev, Y. D., and J. D. C. Craig, 2013: Rotating shallow water turbulence: Experiments with altimetry. *Phys. Fluids*, 25, 106603, https://doi.org/10.1063/1.4826477.

Batchelor, G. K., 1969: Computation of the energy spectrum in homogeneous two-dimensional turbulence. *Phys. Fluids*, 12, II-233–II-239, https://doi.org/10.1063/1.1692443.

Beron-Vera, F. J., 2021: Multilayer shallow-water model with stratification and shear. Rev. Mex. Fis., 67, 351–364, https:// doi.org/10.31349/RevMexFis.67.351.

Bleck, R., S. Benjamin, J. Lee, and A. E. MacDonald, 2010: On the use of an adaptive, hybrid-isentropic vertical coordinate

- in global atmospheric modeling. *Mon. Wea. Rev.*, **138**, 2188–2210, https://doi.org/10.1175/2009MWR3103.1.
- Boffetta, G., and S. Musacchio, 2010: Evidence for the double cascade scenario in two-dimensional turbulence. *Phys. Rev. E*, 82, 016307, https://doi.org/10.1103/PhysRevE.82.016307.
- Callies, J., and R. Ferrari, 2013: Interpreting energy and tracer spectra of upper-ocean turbulence in the submesoscale range (1–200 km). *J. Phys. Oceanogr.*, 43, 2456–2474, https://doi.org/ 10.1175/JPO-D-13-063.1.
- Cho, J. Y.-K., and L. M. Polvani, 1996: The emergence of jets and vortices in freely evolving, shallow-water turbulence on a sphere. *Phys. Fluids*, 8, 1531–1552, https://doi.org/10.1063/1. 868929.
- Cox, M. D., and K. Bryan, 1984: A numerical model of the ventilated thermocline. *J. Phys. Oceanogr.*, 14, 674–687, https://doi.org/10.1175/1520-0485(1984)014<0674:ANMOTV>2.0.CO;2.
- Dossa, A. N., A. C. Silva, A. Chaigneau, G. Eldin, M. Araujo, and A. Bertrand, 2021: Near-surface western boundary circulation off northeast Brazil. *Prog. Oceanogr.*, 190, 102475, https://doi.org/10.1016/j.pocean.2020.102475.
- Dubos, T., and N. K.-R. Kevlahan, 2013: A conservative adaptive wavelet method for the shallow water equations on staggered grids. *Quart. J. Roy. Meteor. Soc.*, 139, 1997–2020, https://doi. org/10.1002/qj.2097.
- —, S. Dubey, M. Tort, R. Mittal, Y. Meurdesoif, and F. Hourdin, 2015: DYNAMICO-1.0, an icosahedral hydrostatic dynamical core designed for consistency and versatility. *Geosci. Model Dev.*, 8, 3131–3150, https://doi.org/10.5194/gmd-8-3131-2015.
- Favier, B., C. Guervilly, and E. Knobloch, 2019: Subcritical turbulent condensate in rapidly rotating Rayleigh–Bénard convection. J. Fluid Mech., 864, R1, https://doi.org/10.1017/jfm.2019.58.
- Ferreira, D., J. Marshall, and J.-M. Campin, 2010: Localization of deep water formation: Role of atmospheric moisture transport and geometrical constraints on ocean circulation. *J. Climate*, 23, 1456–1476, https://doi.org/10.1175/2009JCLI3197.1.
- —, and B. Rose, 2011: Climate determinism revisited: Multiple equilibria in a complex climate model. *J. Climate*, **24**, 992–1012, https://doi.org/10.1175/2010JCLI3580.1.
- Flierl, G.R., and C. S. Davis, 1993: Biological effects of Gulf Stream meandering. J. Mar. Res., 51, 529–560, https://doi.org/ 10.1357/0022240933224016.
- Ford, R., 1994: Gravity wave radiation from vortex trains in rotating shallow water. J. Fluid Mech., 281, 81–118, https://doi.org/10.1017/S0022112094003046.
- Fu, L.-L., and G. R. Flierl, 1980: Nonlinear energy and enstrophy transfers in a realistically stratified ocean. *Dyn. Atmos. Oceans*, 4, 219–246, https://doi.org/10.1016/0377-0265(80)90029-9.
- Garrett, C. J., and W. Munk, 1972: Space–time scales of internal waves. *Geophys. Astrophys. Fluid Dyn.*, 3, 225–264, https:// doi.org/10.1080/03091927208236082.
- —, and —, 1975: Space–time scales of internal waves: A progress report. *J. Geophys. Res.*, **80**, 291–297, https://doi.org/10.1029/JC080i003p00291.
- Grant, H. L., R. W. Stewart, and A. Moilliet, 1962: Turbulence spectra from a tidal channel. *J. Fluid Mech.*, 12, 241–268, https://doi.org/10.1017/S002211206200018X.
- Jackson, L., C. W. Hughes, and R. G. Williams, 2006: Topographic control of basin and channel flows: The role of bottom pressure torques and friction. J. Phys. Oceanogr., 36, 1786–1805, https://doi.org/10.1175/JPO2936.1.
- Julien, K., A. Rubio, I. Grooms, and E. Knobloch, 2012: Statistical and physical balances in low Rossby number Rayleigh–Bénard

- convection. *Geophys. Astrophys. Fluid Dyn.*, **106**, 392–428, https://doi.org/10.1080/03091929.2012.696109.
- —, E. Knobloch, and M. Plumley, 2018: Impact of domain anisotropy on the inverse cascade in geostrophic turbulent convection. *J. Fluid Mech.*, 837, R4, https://doi.org/10.1017/jfm. 2017.894.
- Kevlahan, N. K.-R., 2021: Adaptive wavelet methods for Earth systems modelling. *Fluids*, 6, 236, https://doi.org/10.3390/ fluids6070236.
- —, and T. Dubos, 2019: Wavetrisk-1.0: An adaptive wavelet hydrostatic dynamical core. *Geosci. Model Dev.*, **12**, 4901–4921, https://doi.org/10.5194/gmd-12-4901-2019.
- —, and F. Lemarié, 2022: Wavetrisk-2.1: An adaptive dynamical core for ocean modelling. *Geosci. Model Dev.*, **15**, 6521–6539, https://doi.org/10.5194/gmd-15-6521-2022.
- —, T. Dubos, and M. Aechtner, 2015: Adaptive wavelet simulation of global ocean dynamics using a new Brinkman volume penalization. *Geosci. Model Dev.*, 8, 3891–3909, https://doi.org/10.5194/gmd-8-3891-2015.
- Kitamura, Y., and K. Ishioka, 2007: Equatorial jets in decaying shallow-water turbulence on a rotating sphere. *J. Atmos. Sci.*, 64, 3340–3353, https://doi.org/10.1175/JAS4015.1.
- Kolmogorov, A. N., 1991: The local structure of turbulence in incompressible viscous fluid for very large Reynolds' numbers. *Proc. Roy. Soc.*, A434, https://doi.org/10.1098/rspa.1991.0075.
- Lapeyre, G., 2017: Surface quasi-geostrophy. Fluids, 2, 7, https://doi.org/10.3390/fluids2010007.
- —, and P. Klein, 2006: Dynamics of the upper oceanic layers in terms of surface quasigeostrophy theory. *J. Phys. Oceanogr.*, 36, 165–176, https://doi.org/10.1175/JPO2840.1.
- Le Corre, M., J. Gula, and A.-M. Tréguier, 2020: Barotropic vorticity balance of the north Atlantic subpolar gyre in an eddyresolving model. *Ocean Sci.*, 16, 451–468, https://doi.org/10.5194/os-16-451-2020.
- Lvov, Y. L., and E. G. Tabak, 2001: Hamiltonian formalism and the Garrett-Munk spectrum of internal waves in the ocean. *Phys. Rev. Lett.*, 87, 168501, https://doi.org/10.1103/PhysRevLett.87. 168501.
- Madec, G., and NEMO Team, 2016: NEMO ocean engine, version 3.6. Note du Pôle de modélisation de l'Institut Pierre-Simon Laplace 27, 386 pp., https://www.nemo-ocean.eu/wp-content/uploads/NEMO\_book.pdf.
- Marshall, J., A. Adcroft, C. Hill, L. Perelman, and C. Heisey, 1997: A finite-volume, incompressible Navier Stokes model for studies of the ocean on parallel computers. *J. Geophys.* Res., 102, 5753–5766, https://doi.org/10.1029/96JC02775.
- —, D. Ferreira, J.-M. Campin, and D. Enderton, 2007: Mean climate and variability of the atmosphere and ocean on an aquaplanet. *J. Atmos. Sci.*, **64**, 4270–4286, https://doi.org/10.1175/2007JAS2226.1.
- Molemaker, M. J., J. C. McWilliams, and I. Yavneh, 2005: Baroclinic instability and loss of balance. J. Phys. Oceanogr., 35, 1505–1517, https://doi.org/10.1175/JPO2770.1.
- Morvan, M., X. Carton, P. L'Hégaret, C. de Marez, S. Corréard, and S. Louazel, 2020: On the dynamics of an idealized bottom density current overflowing in a semi-enclosed basin: Mesoscale and submesoscale eddies generation. *Geophys. Astrophys. Fluid Dyn.*, 114, 607–630, https://doi.org/10.1080/03091929.2020.1747058.
- Munk, W., 1950: On the wind-driven ocean circulation. J. Atmos. Sci., 7, 80–93, https://doi.org/10.1175/1520-0469(1950)007<0080: OTWDOC>2.0.CO:2.

- Nadiga, B. T., 2014: Nonlinear evolution of a baroclinic wave and imbalanced dissipation. J. Fluid Mech., 756, 965–1006, https:// doi.org/10.1017/jfm.2014.464.
- Nastrom, G. D., and K. S. Gage, 1985: A climatology of atmospheric wavenumber spectra of wind and temperature observed by commercial aircraft. *J. Atmos. Sci.*, **42**, 950–960, https://doi.org/10.1175/1520-0469(1985)042<0950:ACOAWS> 2.0.CO:2.
- Perruche, C., P. Rivière, G. Lapeyre, X. Carton, and P. Pondaven, 2011: Effects of surface quasi-geostrophic turbulence on phytoplankton competition and coexistence. *J. Mar. Res.*, 69, 105–135, https://doi.org/10.1357/002224011798147606.
- Philander, S., 2001: Atlantic Ocean equatorial currents. Encyclopedia of Ocean Sciences, J. H. Steele, K. K. Turekian, and S. A. Thorpe, Eds., Academic Press, 188–191, https://doi.org/10.1006/rwos.2001.0361.
- Phillips, N. A., 1954: Energy transformations and meridional circulations associated with simple baroclinic waves in a two-level, quasi-geostrophic model. *Tellus*, 6, 273–286, https://doi.org/10.1111/j.2153-3490.1954.tb01123.x.
- ——, 1963: Geostrophic motion. Rev. Geophys., 1, 123–176, https://doi.org/10.1029/RG001i002p00123.
- Rhines, P. B., 1975: Waves and turbulence on a beta-plane. J. Fluid Mech., 69, 417–443, https://doi.org/10.1017/S0022112075001504.
- Rivière, P., A. M. Treguier, and P. Klein, 2004: Effects of bottom friction on nonlinear equilibration of an oceanic baroclinic jet. J. Phys. Oceanogr., 34, 416–432, https://doi.org/10.1175/ 1520-0485(2004)034<0416:EOBFON>2.0.CO;2.
- Rubio, A. M., K. Julien, E. Knobloch, and J. B.Weiss, 2014: Upscale energy transfer in three-dimensional rapidly rotating turbulent convection. *Phys. Rev. Lett.*, 112, 144501, https://doi.org/10.1103/PhysRevLett.112.144501.
- Salmon, R., 1998: Lectures on Geophysical Fluid Dynamics. Oxford University Press, 378 pp.
- Scott, R. K., and L. M. Polvani, 2007: Forced-dissipative shallow-water turbulence on the sphere and the atmospheric circulation of the giant planets. *J. Atmos. Sci.*, 64, 3158–3176, https://doi.org/10.1175/JAS4003.1.
- Smith, K., and G. Vallis, 2001: The scales and equilibration of midocean eddies: Freely evolving flow. *J. Phys. Oceanogr.*, 31, 554–571, https://doi.org/10.1175/1520-0485(2001)031<0554: TSAEOM>2.0.CO;2.
- Steele, J. H., K. K. Turekian, and S. A. Thorpe, Eds., 2001: *Encyclopedia of Ocean Sciences*. Academic Press, 3399 pp.
- Stewart, A. L., J. C. McWilliams, and A. Solodoch, 2021: On the role of bottom pressure torques in wind-driven gyres. *J. Phys.*

- Oceanogr., **51**, 1441–1464, https://doi.org/10.1175/JPO-D-20-0147.1.
- Stommel, H., 1948: The westward intensification of wind-driven ocean currents. Eos, Trans. Amer. Geophys. Union, 29, 202– 206, https://doi.org/10.1029/TR029i002p00202.
- —, 2020: The Gulf Stream. University of California Press, 264 pp. Straub, D. N., and B. T. Nadiga, 2014: Energy fluxes in the quasi-geostrophic double gyre problem. J. Phys. Oceanogr., 44, 1505–1522, https://doi.org/10.1175/JPO-D-13-0216.1.
- Sukhatme, J., and R. T. Pierrehumbert, 2002: Surface quasigeostrophic turbulence: The study of an active scalar. *Chaos*, 12, 439–450, https://doi.org/10.1063/1.1480758.
- Talley, L., 2011: Descriptive Physical Oceanography: An Introduction. Academic Press, 560 pp.
- Theiss, J., 2004: Equatorward energy cascade, critical latitude, and the predominance of cyclonic vortices in geostrophic turbulence. *J. Phys. Oceanogr.*, **34**, 1663–1678, https://doi.org/10. 1175/1520-0485(2004)034<1663:EECCLA>2.0.CO;2.
- Tulloch, R., and K. S. Smith, 2009: Quasigeostrophic turbulence with explicit surface dynamics: Application to the atmospheric energy spectrum. J. Atmos. Sci., 66, 450–467, https:// doi.org/10.1175/2008JAS2653.1.
- Vallis, G. K., 2006: Atmospheric and Oceanic Fluid Dynamics. Cambridge University Press, 1000 pp.
- Wieczorek, M., and M. Meschede, 2018: SHTools—Tools for working with spherical harmonics. *Geochem. Geophys. Geo*syst., 19, 2574–2592, https://doi.org/10.1029/2018GC007529.
- Wunsch, C., 1998: The work done by the wind on the oceanic general circulation. *J. Phys. Oceanogr.*, **28**, 2332–2340, https://doi.org/10.1175/1520-0485(1998)028<2332:TWDBTW>2.0.CO;2.
- Xu, Y., and L.-L. Fu, 2011: Global variability of the wavenumber spectrum of oceanic mesoscale turbulence. J. Phys. Oceanogr., 41, 802–809, https://doi.org/10.1175/2010JPO4558.1.
- —, and —, 2012: The effects of altimeter instrument noise on the estimation of the wavenumber spectrum of sea surface height. *J. Phys. Oceanogr.*, **42**, 2229–2233, https://doi.org/10.1175/JPO-D-12-0106.1.
- Yoden, S., and M. Yamada, 1993: A numerical experiment on two-dimensional decaying turbulence on a rotating sphere. *J. Atmos. Sci.*, **50**, 631–644, https://doi.org/10.1175/1520-0469(1993) 050<0631:ANEOTD>2.0.CO:2.
- Yuan, L., and K. Hamilton, 1994: Equilibrium dynamics in a forceddissipative f-plane shallow-water system. J. Fluid Mech., 280, 369–394, https://doi.org/10.1017/S0022112094002971.